Title
Magnetoelectric Effect and Magnetodielectric Effect in Magnetic Nanoparticles

Author
Kim, Hyungsuk

Publication Date
2013

Peer reviewed|Thesis/dissertation

UNIVERSITY OF CALIFORNIA

Los Angeles

Magnetoelectric Effect and Magnetodielectric Effect in Magnetic Nanoparticles

A dissertation submitted in partial satisfaction of the
requirements for the degree Doctor of Philosophy
in Materials Science and Engineering

by

Hyungsuk Kim

2013

ABSTRACT OF THE DISSERTATION

Magnetoelectric Effect and Magnetodielectric Effect

in Magnetic Nanoparticles

by

Hyungsuk Kim

Doctor of Philosophy in Materials Science & Engineering

University of California, Los Angeles, 2012

Professor Gregory P. Carman

Nano-sized magnetic particles represent considerable interests in modern science because their properties are advantageous to applications such as data storage and medical science. In particular, superparamagnetism is a magnetic property which is found in nano-sized (approximately less than 20 nm) ferromagnetic or ferrimagnetic particles. Studies have shown that superparamagnetic material shows ferromagnetic magnetization only with

an external magnetic field; without an external magnetic field, it loses magnetic properties even at ambient temperature overcoming its intrinsic anisotropy energy. From a magnetic memory standpoint, as bit size decreases, superparamagnetism is a major obstacle to thermal stability due to this volatility, resulting in a loss of information. If it is possible to modulate the superparamagnetic properties of magnetic nanoparticles, this might provide a solution to this critical issue.

In this dissertation, we studied the modulation of superparamagnetic properties by applying an electric field on a magnetoelectric composite composed of magnetic nanoparticles and a piezoelectric substrate. The magnetoelectric effect might present an additional solution to memory device in terms of reducing writing energy by using an electric field rather than an electric current. Additionally, for systems lacking a significant magnetoelectric coupling (for instance, magnetic nanoparticles incased in polymer resin), the relationship between the dielectric constant, which is intrinsically related to ferroelectric order, and magnetic anisotropy energy was investigated.

This dissertation consists of five chapters that discuss the following topics. Chapter 1 introduces the necessary concepts of magnetoelectric (ME) effect, superparamagnetism (SP) and magnetodielectric (MD) effect reviewing previous literature and presents what these research aim to achieve. Chapter 2 briefly presents different

methods for fabricating nanostructures which were investigated in this dissertation. Chapter 3 reports magnetoelectric control of superparamagnetic properties in magnetoelectric composite. Chapter 4 provides magnetodielectric effect in light of magnetic anisotropy energy. Conclusion is presented in Chapter 5.

The dissertation of Hyungsuk Kim is approved.

_____

Sarah H. Tolbert

_____

Yong Chen

_____

Christopher S. Lynch

_____

Gregory P. Carman, Committee Chair

University of California, Los Angeles

2013

This dissertation is dedicated to my family.

Table of Contents

List of Figures

Acknowledgments

First of all, I would like to thank Prof. Greg Carman for accepting me into the lab and guiding me through. Additionally what I have done could not have been possible without the help from my labmates in Active Materials Lab. The names are Kyle Wetzlar, Josh Hockel, Scott Keller, Paul Nordeen, Ray Hsu, Tao Wu, K.P. Mohanchandra and Alex Bur. One last person that I would like to mention is Laura Schelhas from the Department of Chemistry and Biochemistry. I would like to thank them all.

The financial supports for the work were received from Air Force Office of Scientific Research (AFOSR) managed by Dr. Byung-Lip (Les) Lee.

VITA

2007	B.S. Materials Science and Engineering, Korea University
2007-2013	Graduate Student Researcher in UCLA

Publications

1) Mike Emmons, Hyungsuk K.D. Kim, Gregory P. Carman, W. Lance Richards, “Magneto-Optic Field Coupling in Optical Fiber Bragg Gratings”, Optical Fiber Technology, Vol 18, Issue 3, May 2012, Pages 157–160

2) Tao Wu, Mingqiang Bao, Alexxandre Bur, Hyungsuk K.D. Kim, Kotekar P. Mohanchandra, Christopher S. Lynch, Gregory P. Carman, “Electrical tuning of metastable dielectric constant of ferroelectric single crystals for low-power electronics”, Applied Physics Letters, 99, 182903, 2011

3) Tao Wu, Alexandre Bur, Kin Wong, Hockel L. Joshua, Chin-Ray Hsu, Hyungsuk K.D. Kim, Kang L. Wang, and Gregory P. Carman, "Electric-poling-induced magnetic anisotropy and electric-field-induced magnetization reorientation in magnetoelectric Ni/(011) PMN-PT," Journal of Applied Physics 109: 07D732.

4) Alexandre Bur, Tao Wu, Joshua Hockel, Chin-Jui Hsu, Hyungsuk K.D. Kim, Tien-Kan Chung, Kin Wong, Kang L. Wang, and Gregory P. Carman, “Strain-induced Magnetization Change of Patterned Ni Ferromagnetic Nanostructures”, Journal of Applied Physics. 109, 123903. 2011.

Presentations

1) Hyungsuk K.D. Kim, Laura T. Schelhas, Scott Keller, Sarah H. Tolbert, Gregory P. Carman, “Modulating Superparamagnetism with Magnetoelastic Anisotropy” MMM/INTERMAG Conference, Chicago, IL, Jan. 2013 (poster)

2) Hyungsuk K.D. Kim, Laura T. Schelhas, Scott Keller, Sarah H. Tolbert, Gregory P. Carman, “Magnetoelectric control of the superparamagnetic limit” UKC2012, Los Angeles, CA, Aug. 2012 (poster)

3) Hyungsuk K.D. Kim, Laura T. Schelhas, Scott Keller, Sarah H. Tolbert, Gregory P. Carman, “Magnetoelectric control of the superparamagnetic limit” ICM2012, Busan, Korea, July. 2012 (poster)

4) Tao Wu, Alexandre Bur, Hyungsuk K.D. Kim, Ping Zhao, and Gregory P. Carman, “Giant electrical control of magnetic properties in magnetoelectric heterostructures using (110) PMN-PT single crystal,” SPIE Smart Structures/NDE, San Diego, CA, Mar. 2011

1. Introduction

Manipulation of material properties by using a magnetic field or an electric field has been an interesting scientific topic for centuries. Especially in recent years, the magnetoelectric effect has received a great deal of attention because it provides new approaches for devices such as antenna, motor or magnetic memory. In this section of the dissertation, a review of the research on the magnetoelectric (ME) effect, superparamagnetism (SP) and the magnetodielectric (MD) effect are presented. These particular concepts are a focus of this dissertation.

1.1. Magnetoelectric Effect

The magnetoelectric effect has attracted a great deal of attention due to its unique ferroelectric and ferromagnetic phenomena. Recently, of particular interest is the magnetoelectric effect in laminate composites due to its relatively large coupling between electrical energy and magnetic energy compared to single phase. A review of the major research pertaining to the magnetoelectric effect as it is exhibited from scales ranging from

bulk composites to the more recent research, of the last 10 years, on how the effect presents in magnetic thin film and magnetic nanostructures.

1.1.1. History of the Magnetoelectric Effect

Magnetoelectric materials are those which contain ferroelectric and ferromagnetic orders, as shown in figure 1. [1] The magnetoelectric effect was first observed by Rontgen in 1888. [2] The term "Magnetoelectric effect" was coined by Debye in 1926 [3] and it took sixty years until Astrov et al. [4] and V.J. Folen et al. [5] detected experimentally the electric field induced magnetization and the magnetic field-induced polarization in Cr_2O_3 respectively.

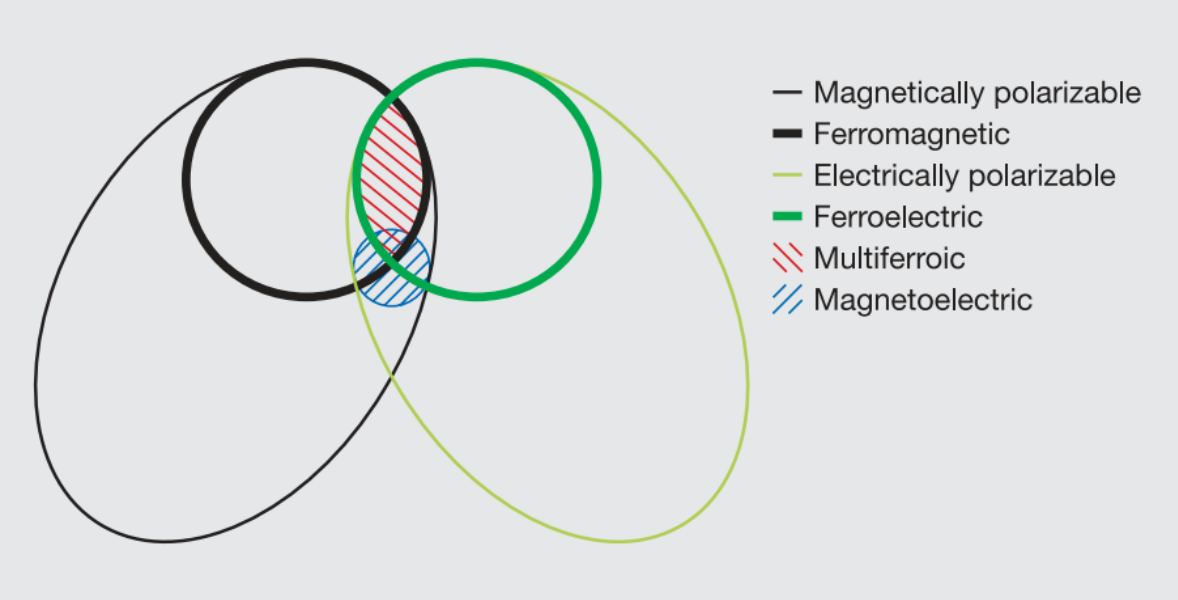

Figure 1. The relationship between multiferroic and magnetoelectric materials [1]

Despite intensive research activities from the turn of the century until the 1970's, efforts made to find strong magnetoelectric coupling between an electric field and a magnetic field in single-phase compounds were futile. [6-9] Additionally, the magnetic transition temperatures, of both the Curie and Néel temperature within single phase magnetoelectrics were far lower than room temperature. This made experimental analysis quite challenging and when compounded by the immense difficulty that fabricating compounds of good quality were in that era, results were sparse and often inconclusive. [10,

11] These difficulties of observing strong correlation between the electrical and magnetic ordering in a single phase compound was averted by the advent of using two or more single phase compounds in composite structures [12-15]; as a transfer mechanism, indirect coupling through extrinsic mechanical strain was suggested. [16] The magnetoelectric effect in a composite can be classified into two categories depending on the input and output. When the input is a magnetic field and the output is an electrical voltage, the term "direct magnetoelectric effect" is used and it is defined by the product property, "$\text{direct magnetoelectric effect (DME)} = \frac{\text{electric}}{\text{mechanical}} \times \frac{\text{mechanical}}{\text{magnetic}}$". [17, 18] In other words, the strain induced by a magnetic field in magnetostrictive materials is passed onto the piezoelectric materials so that as a result the induced change of electric polarization is measured. The idea of DME is essential from the magnetoelectric magnetic field sensor point of view. When the process is performed in reverse, the term "converse magnetoelectric effect (CME)" is used. [18, 19] For CME, the input, an electric field, induces mechanical strain in the piezoelectric material and the electric field induced strain affects the alignment of the magnetizations in the magnetostrictive material. CME opens up the possibility of intrinsic control of magnetization with an electric field.

The research on the the magnetoelectric effect in a composite started with particulate composites where the magnetoelectric voltage coefficients were larger than

those of single-phase compounds by more than an order of magnitude. [13, 14, 16] However, due to the issues such as possible chemical reaction between the piezoelectric and magnetostrictive materials during sintering processes and the potential of mechanical defects caused by lattice mismatch, the magnetoelectric voltage coefficients of the particulate composites were well below the theoretically expected values. These were avoided by using laminate composites consisting of ferroelectric and ferromagnetic plates. In 2001, Ryu et al. [20] reported magnetoelectric effect in laminate composites by combining a Terfenol-D (magnetostrictive material) plate and a ferroelectric PZT (lead zirconate titanate, $Pb[Zr_xTi_{1-x}]O_3$ $0 \leq x \leq 1$) plate with silver epoxy. Ryu et al's sample is shown in figure 2.

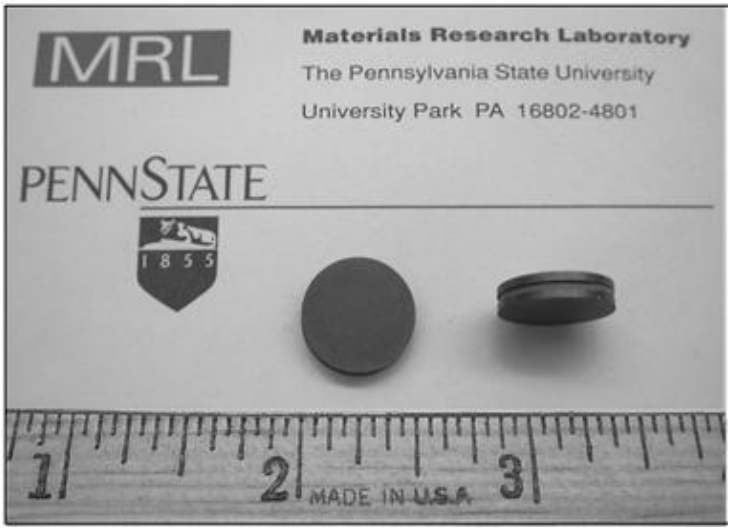

Figure 2. Magnetoelectric composite (PZT sandwiched by Terfenol-D) [20]

While subsequent reports dealt with bulk property measurements [19, 21-24], the last 5 years have seen a surge in research on the control of nanoscale domain structures through the magnetoelectric effect. In the following sections, 1.1.2 and 1.1.3, literature reviews on magnetoelectric effect in thin film and nanostructures are presented, which will help understand the advances in the area which led to this dissertation.

1.1.2. Magnetoelectric Effect in Thin film

For single phase magnetoelectric thin film, $BiFeO_3$ (BFO) has been a focus of attention due to its high operating temperature compared to most single phase magnetoelctrics. Wang et al [25] deposited epitaxial $BiFeO_3$ (BFO) multiferroic (ferroelectric (T_C ~1103 K) and antiferromagnetic (T_N ~643 K)) onto single crystal $SrTiO_3$ (100) substrates by pulsed laser deposition. The 50~500 nm thick BFO thin films show enhanced ferroelectric and ferromagnetic properties with large spontaneous polarization compared to those of bulk BFO.

In the case of composite magnetoelectric thin film, Liu et al [26, 27] and Li et al [28] demonstrated strong magnetoelectric coupling in ferrite thin film on a piezoelectric substrate, PZN–PT (lead zinc niobate–lead titanate). Figure 3 shows that magnetization of ferrite thin film changes 90 degree in in-plane direction due to electric field induced strain from piezoelectric substrate. [27]

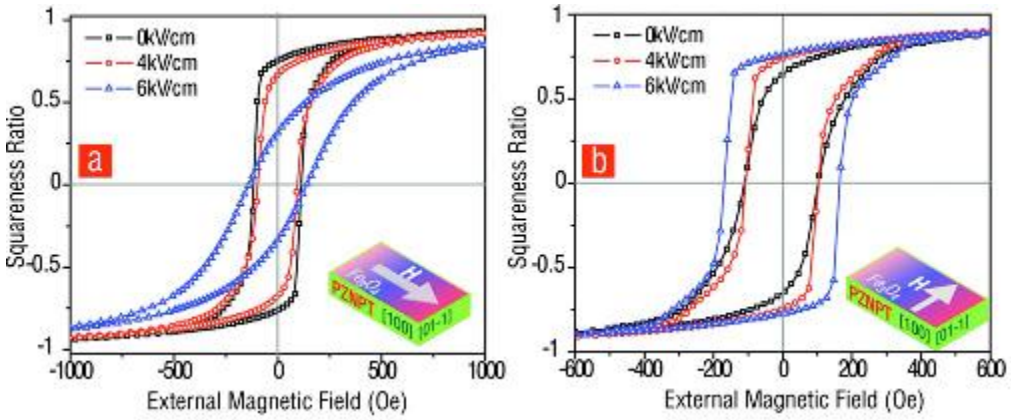

Figure 3. Magnetic hysteresis loop of Fe3O4/PZN-PT changes according to the electric field applied [27]

Zheng et al [29] reported the magnetoelectric coupling between perovskite $BaTiO_3$ and spinel $CoFe_2O_4$ on 2-2 (horizontal heterostructure) as well as 1-3 (vertical heterostructure) structure types fabricated on top of SrRuO. Figure 4 (B) shows alternating layers of the ferroelectric phase ($BaTiO_3$) and the ferromagnetic/ferrimagnetic phase ($CoFe_2O_4$) and a heterostructure consisting of nanopillars of the ferromagnetic/ferrimagnetic phase embedded in the ferroelectric phase is illustrated in figure 4 (D). The latter configuration exhibited stronger magnetoelectric coupling due to the reduced clamping effect from the substrate.

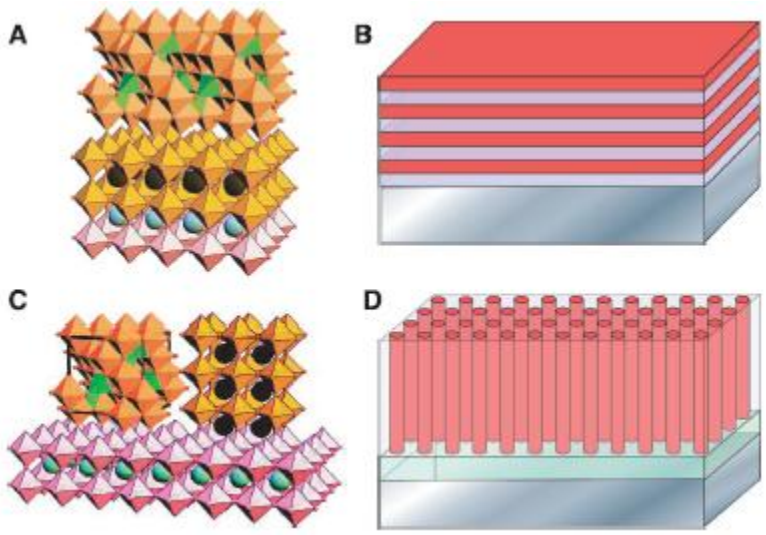

Figure 4. (A-B): 2-2 magnetoelectric composite with alternating layer having spinel and perovskite structures. (C-D): 1-3 magnetoelectric composite with spinel nanopillars surrounded by perovskite matrix [29]

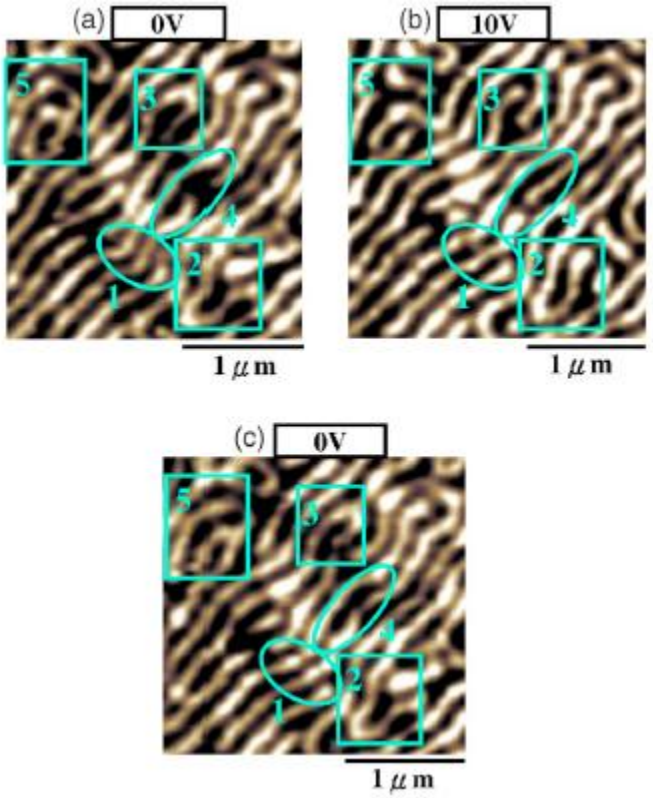

Figure 5. MFM images of electrical control of magnetic domain pattern in thin film Ni/PZT/Si taken at 0 and 10 V [23]

In 2008, Chung et al. [23] reported reversible magnetic stripe domain-wall motion under an applied electric field in a bilayer consisting of thin film ferromagnetic (Ni, 100 nm thick)/ferroelectric (PZT, 1.28 micron thick)/Si (500 micron thick) heterostructure using

magnetic force microscopy. Figure 5 shows MFM images of magnetic stripe domain patterns before (figure 5 (a)) and after (figure 5 (b)) applying 10 V of an electric field. When the electric field is removed, the magnetic domain patterns return to their original position, figure 5 (c). The observed magnetic change was limited due to the clamping effect from the thick Si substrate. Wu et al. [30-32] avoided the clamping effect by depositing magnetic thin film on top of the piezoelectric substrate in 2011 as shown in figure 6, demonstrating reversible and metastable magnetic anisotropy reorientation in a magnetoelectric polycrystalline Ni thin film and (011)-oriented $[Pb(Mg_{1/3}Nb_{2/3})O_3]_{(1-x)}$–$[PbTiO_3]_x$ (PMN-PT) heterostructure. The change is attributed to remanent strain from PMN-PT when operating the PMN-PT in a non-linear strain states (B-E in the inset in figure 6). The fact that reported changes in magnetization states are stable without the application of an electric field and can be modulated by an electric field opens new avenues for a number of applications, especially useful to information technology.

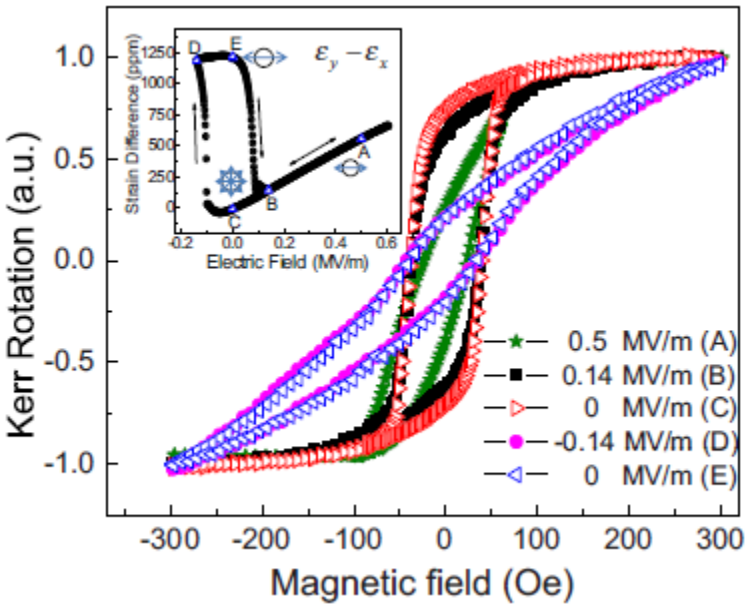

Figure 6. Normalized magnetic hysteresis curves measured with Magneto-Optical Kerr Effect device (MOKE) along the y direction where relatively larger strain is induced compared to x direction under different electric fields. (A) - (E) represent the labeled strain states in the inset. The inset shows in-plane strain difference as a function of electric field. [30]

1.1.3. Magnetoelectric Effect in Magnetic Nanostructures

It was not until 2005 that research on ME effect in nanostructures was carried out. In 2005, Zavaliche et al. [21] proposed an electric field assisted magnetization control in terms of magnetic random access memory (MRAM) application showing room-temperature magnetization reversal induced by an electric field in epitaxial ferroelectric $BiFeO_3$-ferrimagnetic $CoFe_2O_4$ columnar nanostructures (thin-film magnetoelectric vertical nanostructures as shown in figure 7. Their follow-up work in 2007 optimized the fabrication of the heterostructure but showed similar results to work published in 2005. [22]

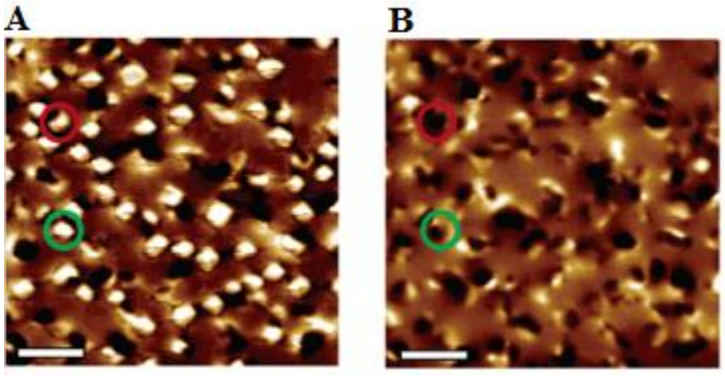

Figure 7. Images showing changes in the magnetic configuration in epitaxial ferroelectric BiFeO3-ferrimagnetic CoFe2O4 columnar nanostructures. (bar : 1 micron)

(A): after magnetizing in a perpendicular direction (B): after electrical poling at +12 V. [21]

In 2008, Chu et al. [33] reported a local magnetic control of ferromagnetic CoFe coupled with $BiFeO_3$ that are both antiferromagnetic and ferroelectric. Chung et al. [34] reported reversible single-domain evolution from an initial single-domain state to a S-shape domain state with an applied electric field in Ni-nanobar attached to magnetoelectric lead zirconate titanate film as shown in figure 8.

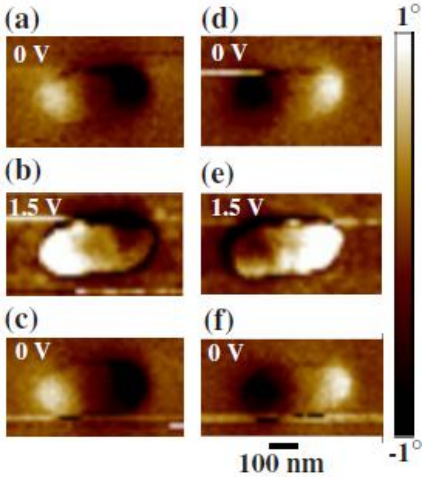

Figure 8. Reversible control of single domain state with an electric field [34]

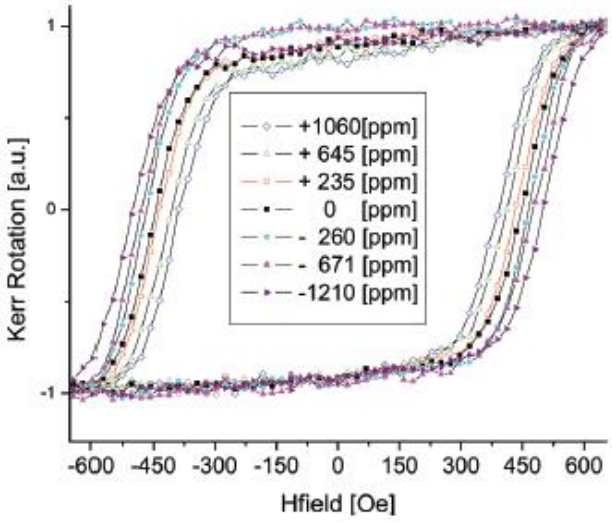

Figure 9. Magnetization (M) - magnetic field (H) curves measured for different relative strain difference between y and x axis [35]

As can be seen in figure 9, Bur et al [35] demonstrated strain-mediated coercive field changes in 300 by 100 by 35 nm^3 Ni nanostructures deposited on Si/SiO2 substrate using four-point bending setup. While the results is in a good agreement with micromagnetic simulation, the change was severely limited compared to figure 6 due to the strong shape anisotropy of the bar type nanostructures.

1.2. Superparamagnetism

In order to introduce the basic concepts of superparamagnetism, the following section reviews the physical origin of the magnetic domain structure, single domain and the thermal origins of superparamagnetism.

1.2.1. Magnetic Domain

The first postulation of the existence of domains was made by Weiss [36] in an attempt to explain the fact that the net magnetization of ferromagnetic materials is zero for bulk materials. Magnetic domain is a basic element of the microstructure of magnetic materials. In ferromagnetic materials, all the magnetic dipoles in each domain are aligned parallel with each other. The magnetization vectors of different domains are not necessarily parallel. Therefore, the total magnetization of ferromagnetic materials is zero on average due to their randomized directionality of the domains.

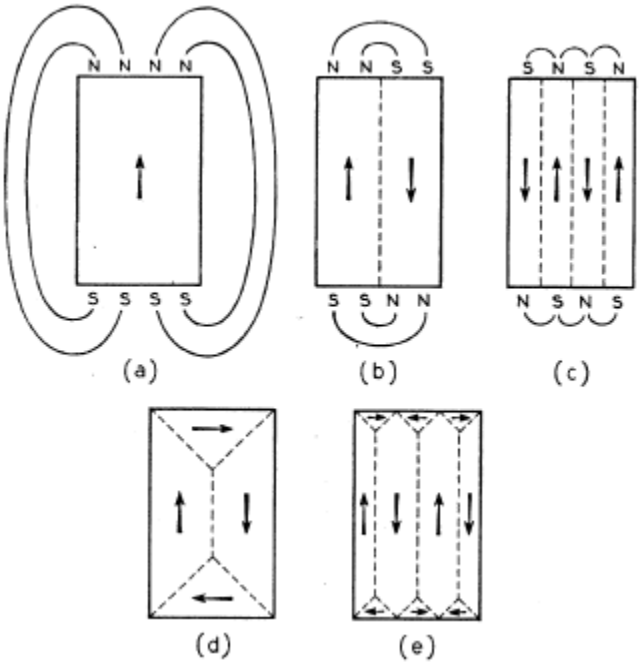

Figure 10. Domains and domain walls. From (a) to (e), the change of domain structure is presented. (Arrow: the magnetization vector. Dashed lines: domain walls) [36]

Figure 10 illustrates the evolution of domain structure from (a) to (e); each picture represents a cross section of a ferromagnetic single crystal. Domain structure of a magnetic material changes to lower the total energy associated with the specimen. The boundary between domains with different magnetic orientations is called a domain wall. In order to decrease the magnetostatic energy formed by north and south poles in figure 10

(a), a domain wall is formed so that each domain has the opposite orientation of magnetization and the magnetostatic energy is reduced roughly by half in figure 10 (b). Note that the magnetostatic energy is volume energy which is proportional to L^3, while the domain wall energy is surface energy which is proportional to L^2. (L: unit length of the magnetic material) In other words, volume energy dominates when the magnetic material consists of large domains so that domain wall formation becomes energetically favorable to reduce the energy associated with it; with a great number of relatively small domains, domain wall formation is not favorable any more due to large surface energy from domains. It indicates the subdivision process continues until the energy to create the domain wall is equal to the reduction in magnetostatic energy. Consequently, the process shown in figure 10 is an energy minimization process between magnetostatic energy and domain wall energy.

Domain structure, which is determined by an energy minimization process, evolves under the application of a magnetic field. It has been shown that the fundamental magnetization process by applying the magnetic field is composed of two mechanisms. [36] One is the growth of domains which have magnetic dipole moment favorably oriented with respect to the applied field at the expense of unfavorably oriented domains by domain wall

movement. The other is the rotation of magnetization close to the direction of an applied magnetic field.

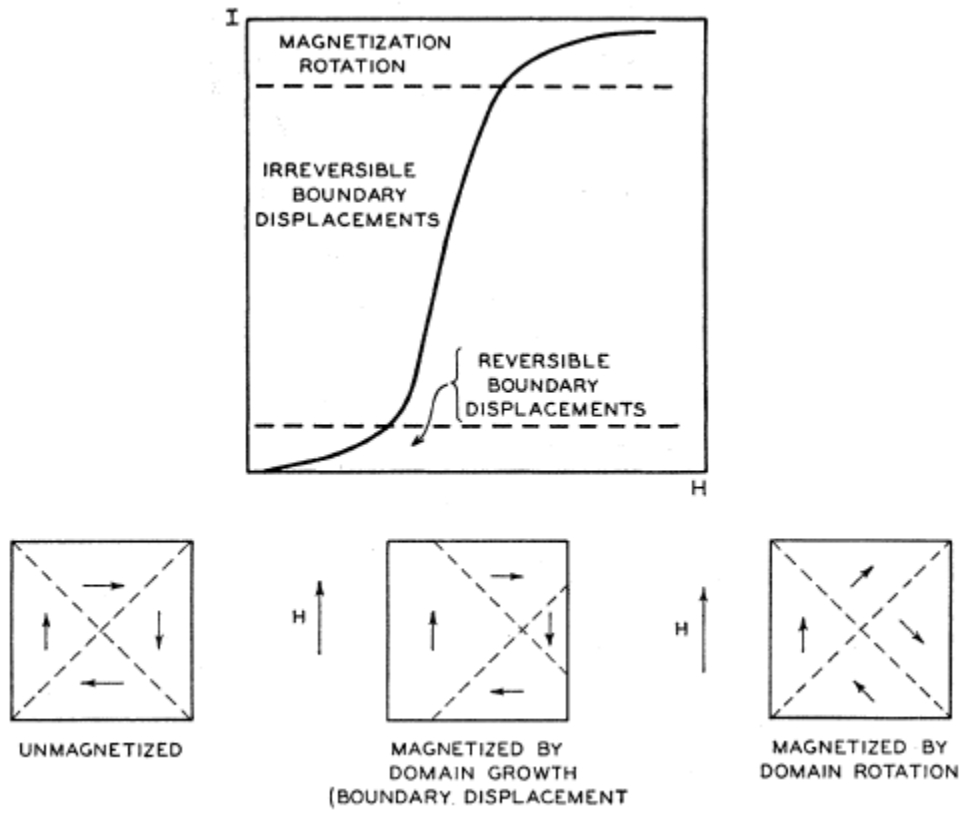

Figure 11. Magnetization curve and magnetization process [36]

In figure 11, a typical magnetization curve is shown for a ferromagnetic material with the regions that are dominated by different processes. In a weak field, the net change of magnetization is controlled by domain wall motion resulting in the evolution of the domain sizes. The magnetization is changed by domain rotation in a strong field.

1.2.2. Single Domain

As dimensions of the ferromagnetic or ferrimagnetic materials are reduced, the surface to volume ratio increases. The energy required to maintain or create domain wall is surface energy, while the magnetostatic energy is volume energy. Therefore, below a critical size, the specimen is composed of a single domain since it represents a minimum energy between domain walls and magnetostatic energy. Frenkel and Dorfman [37] theoretically predicted the single domain state in 1930 and the Kittel [38] calculated an estimated size for it.

In nano-sized materials, magnetic anisotropy energy becomes a dominant factor in the magnetic domain formation. The magnetic anisotropy energy is related to the

dependence of magnetization direction on the various sources such as crystalline structure, physical shape, or mechanical strain. In other words, magnetic anisotropy energy tends to arrange magnetizations along certain axes; the direction favored by the anisotropy energy is called a preferred or easy axis. Suppose there is a uniaxial single domain particle. Figure 12 shows the energy well associated with anisotropy energy of single domain magnetic material. [39] Anisotropy energy is given by $E = KV\sin^2\theta$ where K is the effective uniaxial anisotropy energy per unit volume, θ is the angle between the magnetization and the easy axis, and V is the volume of particle. [40] In order to move the magnetization away from the easy axis, anisotropy energy needs to be overcome by the external energy.

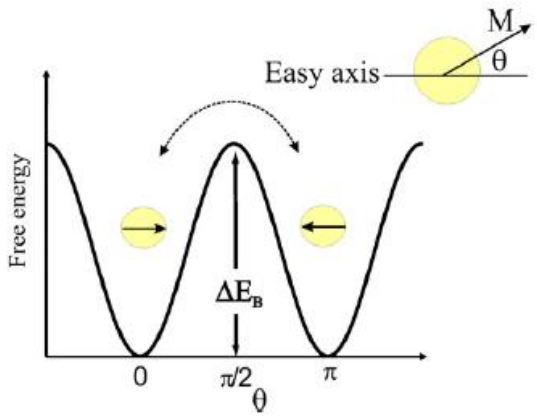

Figure 12. Illustration of uniaxial single domain particle and anisotropy energy

depending on the angle between the magnetization and the easy axis [39]

1.2.3. Superparamagnetism

In a ferromagnetic or ferrimagnetic nanoparticle whose size is smaller than single domain, thermal energy can become the dominant quantity over the magnetic anisotropy energy. The nanoparticle which is less than ~20 nm diameter may lose net magnetization due to their randomized motion above the, so-called, blocking temperature. This state is called superparamagnetic.

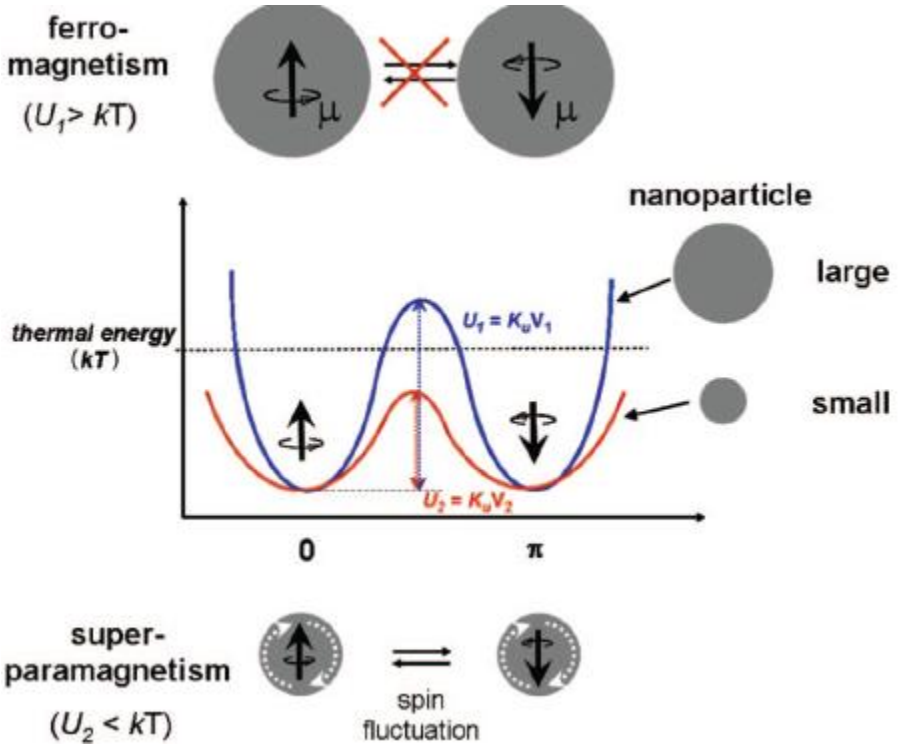

Figure 13. Schematic energy diagram of magnetic nanoparticles with factors such as different sizes and temperatures [41]

Figure 13 shows the energy well diagram of magnetic nanoparticles. While relatively large nanoparticles (upper curve) have magnetic anisotropy that is larger than thermal energy (kT), relatively small nanoparticles (lower curve) have magnetic anisotropy barrier which is less than thermal energy. This dominating thermal energy for small

nanoparticles leads to the random fluctuation of the magnetizations, resulting in a net loss of magnetizations.

Above the blocking temperature, the material in a bulk form would show net magnetization because the blocking temperature is less than Curie temperature; for example, the blocking temperature of a 16 nm Ni nanoparticle is 300 K while the Curie temperature of bulk Ni is 628 K. It demonstrates superparamagnetism is a phenomenon which can be found in magnetic nanoelements. [40-44] For superparamagnetic materials, even at temperature below Curie temperature, thermal energy above blocking temperature is high enough to make the dipoles move randomly making them lose magnetic properties. However, once magnetized, they become magnetic with extremely high susceptibility, which is a unique characteristic compared to paramagnetism.

Superparamagnetism was predicted by Néel [45] and the term was coined by Bean [46] based on the similarity and difference when compared with paramagnetism. The similarity between superparamagnetism and paramagnetism is that both materials show a magnetic response only with an external magnetic field applied. The difference is that superparamagnetic materials have a much greater magnetic susceptibility. Even with a very small magnetic field, ferromagnetic materials below Curie temperature show appreciable magnetization due to mutual interaction also known as the quantum mechanical

exchange force as illustrated in figure 14. Magnetic dipoles in a superparamagnetic nanoparticle are interacting mutually by quantum mechanical exchange force; note that superparamagnetism is basically nanoscale phenomenon of ferromagnetism or ferrimagnetism. For paramagnetism, magnetic moments are independent and each magnetic dipole needs its own magnetic field to overcome thermal energy. This is the reason why paramagnetic materials show linear relationship between magnetization and an applied magnetic field, while superparamagnetic nanoparticles show a nonlinear relationship as shown in figure 15.

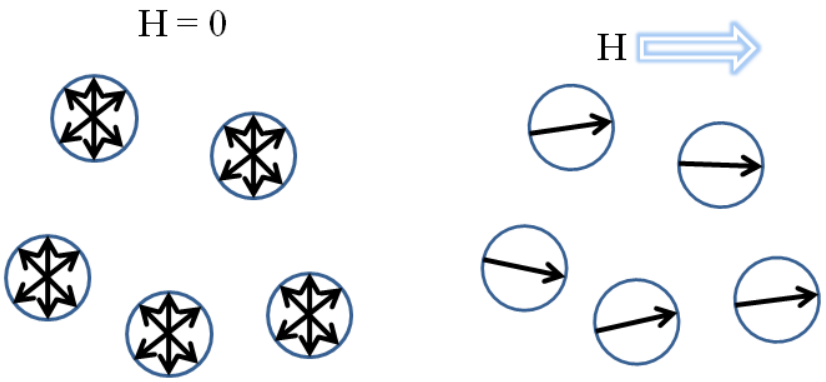

(a) (b)

Figure 14. Schematic description of magnetization of superparamagnetic nanoparticles with (b) and without (a) an applied magnetic field

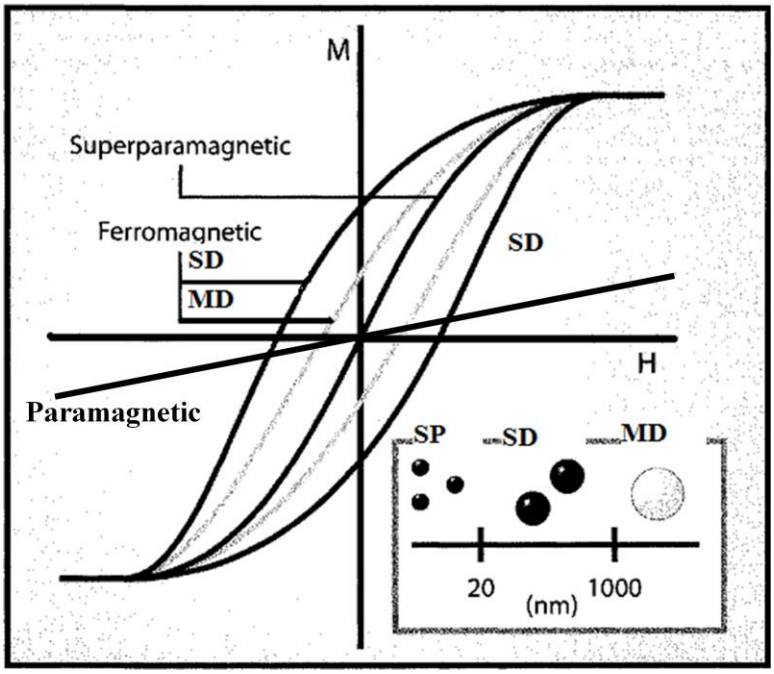

Figure 15. Hysteresis curves depending on the particle sizes [47]

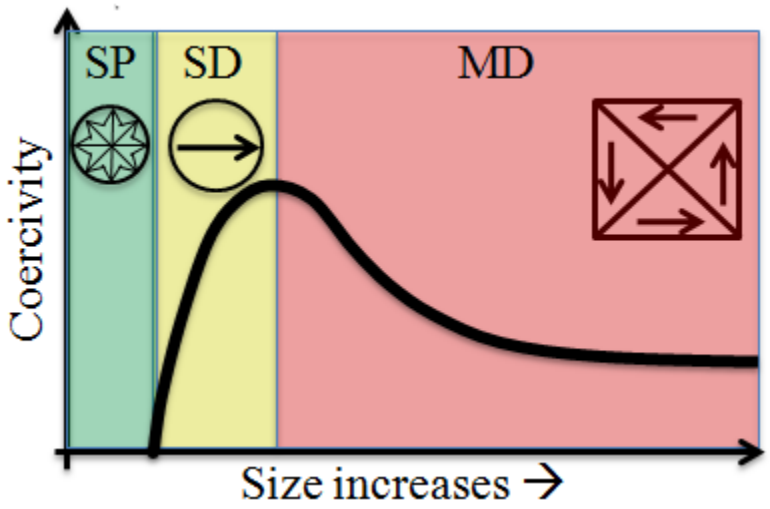

Figure 16. Coercivity depending on the sizes of magnetic materials

The magnitude of coercive field relies on the size of the magnetic materials. Figure 16 helps illuminate the correlation between coercivity and particle size in ultrafine particles. For a nanoelement composed of a single domain, magnetic dipoles lie in an easy axis direction subjected to anisotropy energy. Hence, in a single domain state (SD), coercivity which is needed to change the direction of magnetization is bigger than in the multi domain materials. Coercivity continuously decreases as the size of nanoparticle gets smaller because the magnitude of magnetic dipole is reduced so that thermal energy affects the

spins more strongly. The particles become superparamagnetic when thermal energy exceeds the magnetocrystalline anisotropy energy of the nanoparticles.

1.2.4. Literature Reviews on Superparamagnetism

Past research on superparamagnetic materials can be classified into three areas, the investigation of fundamental superparamagnetic properties, biomedical application and improving the thermal stability of superparamagnetic nanoparticle for memory application. In this section, the representative research associated with these three areas is presented.

In 1998, Chen et al [48] did the exemplary study on the fundamental superparamagnetic properties of $MgFe_2O_4$ spinel ferrite nanoparticles by varying different parameters such as a particle size, temperature and a magnetic field.

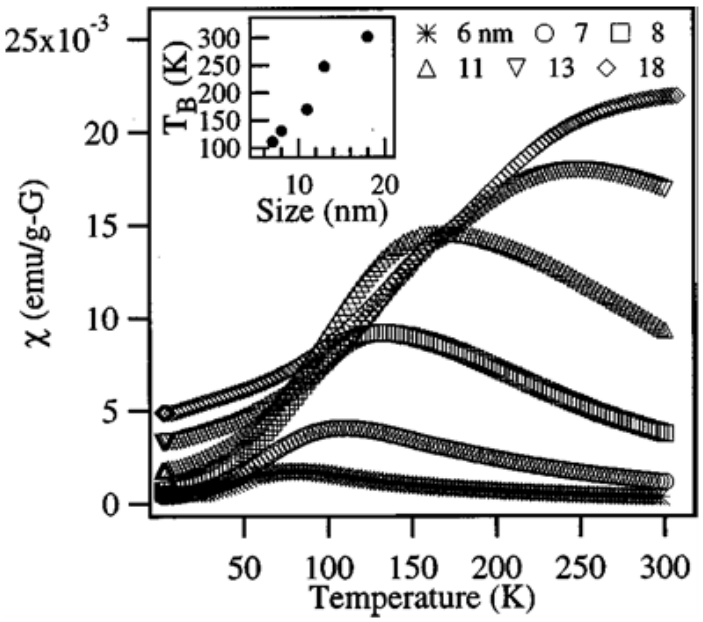

Figure 17. Magnetic susceptibility depending on temperature with different sizes for $MgFe_2O_4$ nanoparticles under the magnetic field of 100 Oe. The inset indicates the relationship between blocking temperature and the size of nanoparticles [48].

Figure 17 shows how the magnetic susceptibility varies with temperature and size of the $MgFe_2O_4$ nanoparticles. The sample was cooled to 1.7 K without a magnetic field and temperature was increased slowly. (Zero Field Cooling measurement, ZFC) Each line in figure 17 has a trend of initial increase and subsequent decrease at a certain

temperature. At 1.7 K, the magnetic moments in particles are “frozen” and aligned along their own easy axis. As temperature increases up under an application of a magnetic field of 100 Oe, there is more fluctuation of magnetization away from an easy axis trying to align magnetization close to the direction of an applied magnetic field; 100 Oe is insufficient to overcome the entire magnetocrystalline anisotropy energy. At a certain temperature, magnetic susceptibility starts to decrease because the thermal energy is large enough to overcome the anisotropy energy so that nanoparticles lose magnetic property due to randomized direction of magnetizations. In other word, at this temperature called the blocking temperature, nanoparticles are superparamagnetic.

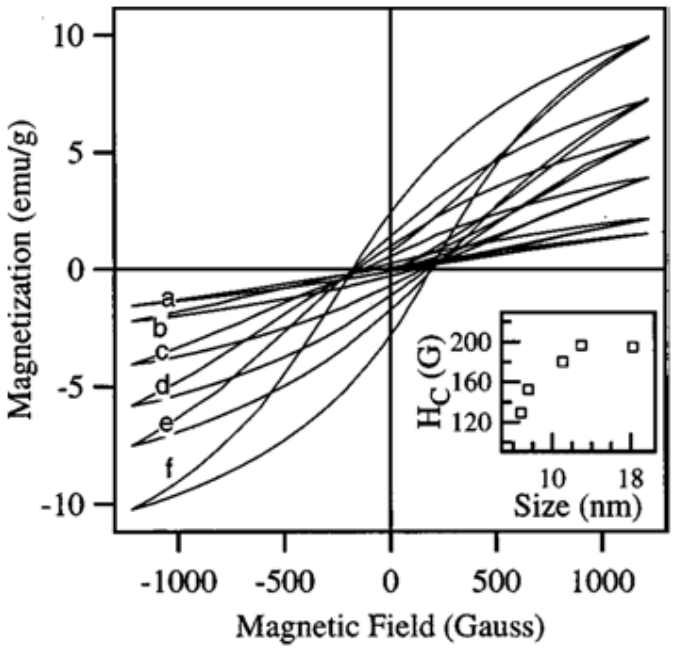

Figure 18. Magnetization depending on a magnetic field for $MgFe_2O_4$ nanoparticles with sizes 6, 7, 8, 11, 13, 18 nm for a, b, c, d, e, f respectively at 50 K. The inset shows relationship between the coercivity and the particle size. [48]

Figure 18 shows the magnetization of nanoparticles at 50 K based on a magnetic field which is below the blocking temperature. As the particle size increases, the hysteresis loop enlarges due to the increase of the coercivity of $MgFe_2O_4$ nanoparticles.

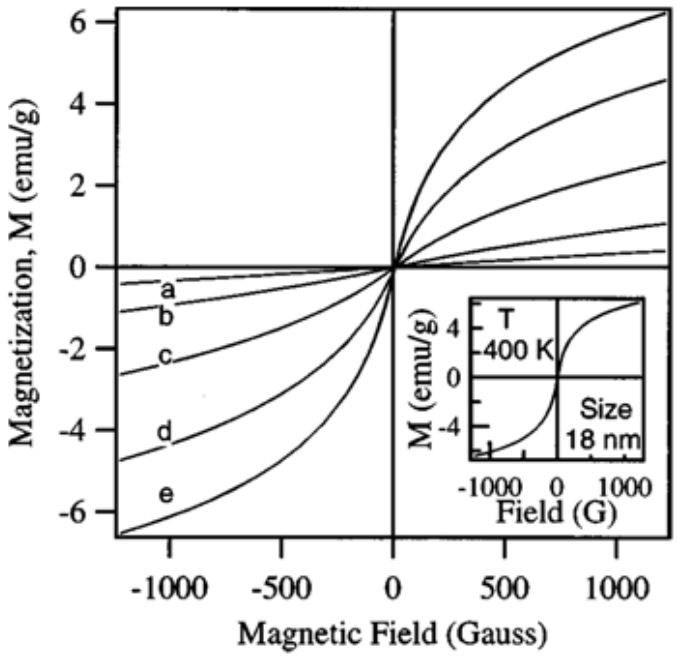

Figure 19. Magnetization depending on a magnetic field for $MgFe_2O_4$ nanoparticles with sizes 6, 7, 8, 11, 13, 18 nm for a, b, c, d, e, f respectively at 300 K. The inset shows the case for nanoparticle with a size of 18 nm at 400 K. [48]

Above blocking temperature, thermal energy overcomes the magnetocrystalline energy and no hysteresis appears for the nanoparticles in figure 19.

The switchable characteristic of superparamagnetic nanoparticles has attracted a lot of consideration in the biomedical area where they are used for drug targeting or as a

contrast agent for magnetic resonance imaging (MRI). [49] In case of drug targeting, a drug which is attached to a superparamagnetic particle is guided by the external magnetic field to the desired location and is held fixed while the medication acts locally. When the process is finished and the external magnetic field is removed, the particles lose magnetic property and are no longer accumulated at the location. [49, 50]

The research on improving thermal instability of superparamagnetic materials has been performed in order to increase the bit capacity of a magnetic random access memory (MRAM) which is considered as a potential candidate for future non-volatile memory devices. Magnetic storage media at present consists of weakly coupled magnetic alloys sputtered on a flat surface, or a platter. Even though one grain is about 10 nm in size, due to random alignment of the grains on a platter, one bit of information needs to be stored in approximately 10 grains to make sure it is properly written. [51] 10 grains make for a magnetic single domain and it responds to an externally applied magnetic field through rotation of magnetization without domain wall motion. It leads to higher coercivity and accordingly higher stability. However, as the bit density increases, ambient thermal energy becomes higher than intrinsic magnetic anisotropies, resulting in loss of information. [52] The size of one bit below which superparamagnetism begins is called superparamagnetic limit and even with recent effort to develop bit-patterned media (BPM) in order to increase

recording density over granular media, the thermal instability problem still comes into play. [51, 53-55] Efforts have been made to overcome this effect by adding additional magnetic anisotropy to superparamagnetic materials such as shape anisotropy or using exchange bias induced when coupled with antiferroamgentic materials. [42, 56, 57]

Cowburn [42] did a preliminary experiment that shows the effect of shape anisotropy on stabilizing magnetic nanoelements over the thermal fluctuation.

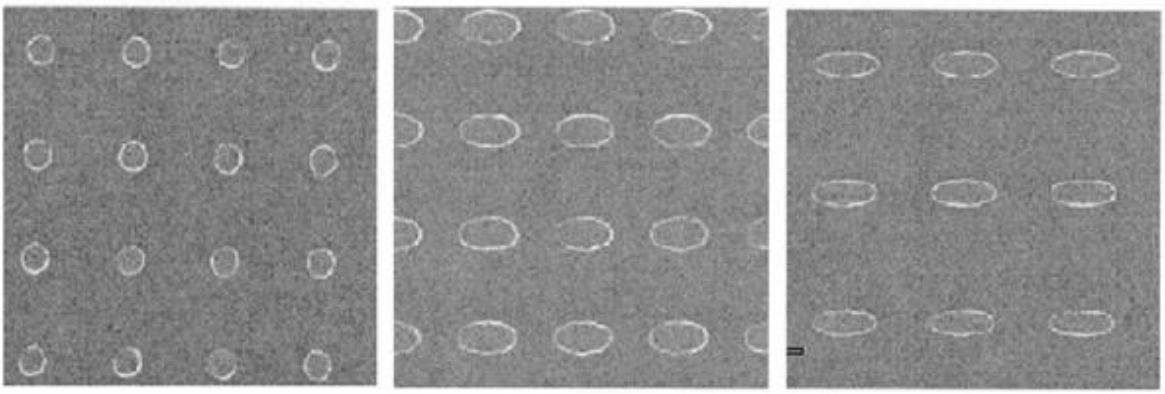

(a) (b) (c)

Figure 20. Scanning electron microscope (SEM) images. Dimensions (nm) :

(a) 75 X 75 X 15; (b) 180 X 90 X 10; (c) 270 X 90 X 10 [42]

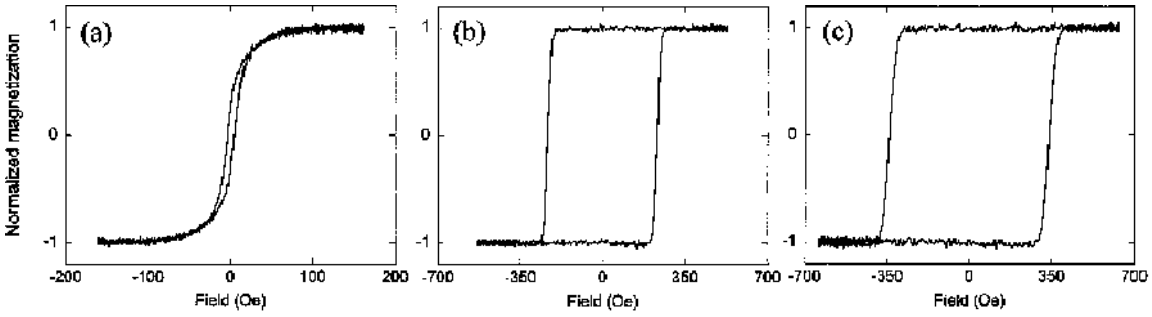

Figure 21. Measured hysteresis loops. Dimensions (nm) :

(a) 90 X 90 X 10; (b) 180 X 90 X 10; (c) 270 X 90 X 10 [42]

Figure 20 shows planar elliptical permalloy nanoelements that were fabricated by electron beam lithography. Their measured hysteresis indicates that as the aspect ratio increased from figure 21 (a) to figure 21 (c) larger coercivity was obtained. In other words, shape anisotropy had a stabilizing effect on the nanoscale elements.

The exchange bias created at the interface between antiferromagnetic and ferromagnetic materials has been used in order to increase the thermal stability of the nanoparticles. Nogues et al [58] showed that the hysteresis curve was shifted when the

ferromagnetic nanoparticles were placed on an antiferromagnetic material. In other words, the exchange bias increased the nanoparticles anisotropy energy. Figure 22 (a) shows spin states of superparamagnetic nanoparticles and a corresponding energy well where the height of the well is the magnetic anisotropy energy. Due to the thermal energy comparable to magnetic anisotropy energy, the magnetization of superparamagnetic nanoparticles can be switched from one easy axis to the other easy axis. Figure 22 (b) illustrates the increased height of the energy well due to the additional anisotropy energy provided by exchange bias, resulting in stabilization of the magnetization in one easy axis. Skumryev et al [56] reported that the blocking temperature of the 3~4 nm Co nanoparitcles embedded in antiferromagnetic CoO matrix was more than two orders of magnitude higher than that of the nanoparticles embedded in paramagnetic matrix.

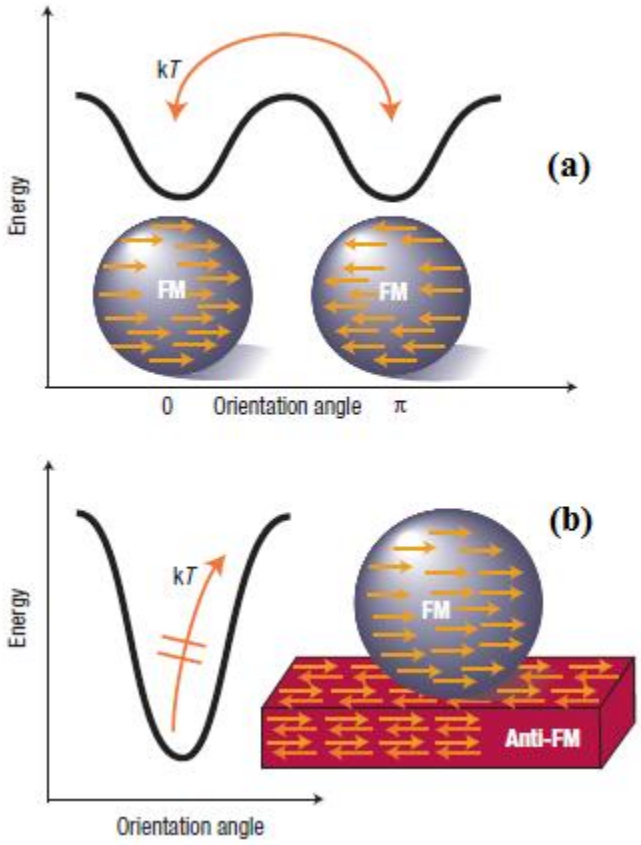

Figure 22. Ferromagnetic nanomagnet is located on the antiferromagnetic surface resulting in stable magnetization [59]

In chapter 3, we present a new approach on improving thermal instability of superparamagnetic materials by adding electric field induced magnetoelastic anisotropy.

1.3. Magnetodielectric Effect

There are two types of magnetoelectric materials; single phase and composite materials. Due to the difficulty in finding single phase magnetoelectric materials with good conversion efficiency between magnetic energy and electrical energy, these days magnetoelectric research focuses on composite magnetoelectric materials. We believe the magnetodielectric research improves our understanding about dielectric property of the single phase magnetoelectric materials, which ultimately can help design single phase magnetoelectric materials with high magnetoelectric conversion constant. In this section, we briefly introduce magnetodielectic effect.

1.3.1. Magnetodielectric Effect

The magnetodielectric (or magnetocapacitance) effect refers to a phenomenon where dielectric constant is controlled by magnetic field. The effect is observed in magnetoelectric materials since the dielectric constant is intrinsically related to electric polarization and indirectly related to the magnetic order. [60-63] However, the magnetodielectric effect can also arise in materials without a net polarization change where

the dielectric constant is due to magneto-resistive effect present in the material. [61] Therefore, the magnetodielectric response can also occur in magnetic materials which are not intrinsically multiferroic but exhibit qualities that are both related as well as potentially useful to the general class of multiferroic materials.

It has been less than 10 years since magnetodielectric effect was reported on single phase magnetoelectric materials. The research on magnetodielectric effect on $BiMnO_3$ by Kimura et al in 2003 was the first of its kind. [62] In 2006, the max value in magnetodielectric constant was found at a temperature which was much less than the Curie temperature. [64] The reason for that has not been provided and we discovered that magnetodielectric constant correlates to magnetic anisotropy at specific temperature. It will be introduced in chapter 4.

2. Fabrication of Nanoscale Ferromagnetic Materials

In this section the fabrication methods for producing magnetic nanostructures below 50 nm is examined. Self-assembled templates (anodic aluminum oxide and di-block copolymer template) are used in addition to chemical synthesis method. Self-assembled template methods have advantages that their costs are cheaper and they can fabricate features over larger areas compared to electron beam lithography methods which are more expensive and time consuming. In addition to those drawbacks, electron beam lithography lacks the capability to produce nanoscale features less than 20 nm due to the electron beam scattering when interacting with photoresist. [65] Chemical synthesis is suitable for mass production and has its own advantages in that it enables the precise control of the nanostructures. [66, 67] The mass production capability for these methods is crucial since, for a single nanoscale multiferroic structure, the total magnetic moment is insufficient to be measured in a macro device such as superconducting quantum interface device (SQUID) or magneto-optic Kerr effect (MOKE) systems. For a 40 nm diameter nanodot with thickness of 10 nm to be detected by SQUID, the most sensitive magnetometer at present, more than 100 million of them are required.

2.1. Anodic Aluminum Oxide

Even though electrochemical oxidation of aluminum garnered a great deal of attention as a corrosion-resistive and decorative coloring on metal surfaces for more than 100 years, it has been less than 20 years since anodic aluminum oxide (AAO) triggered much activity as a template for fabricating nanodots and nanowires in a highly ordered array. [68-72] It has been reported that by varying the anodization conditions such as solutions, voltages applied and temperatures, pore diameter (20 to 100 nm) and interpore distance can be controlled. Generally, pore size and interpore distance increases linearly with voltage applied during anodization as can be seen in figure 23. [73-75] In a nanodot fabrication process, an aluminum thin film is anodized after being evaporated on the substrate. The desired material is deposited through pores in the alumina template. When AAO is removed [76], there remains an array of nanodots.

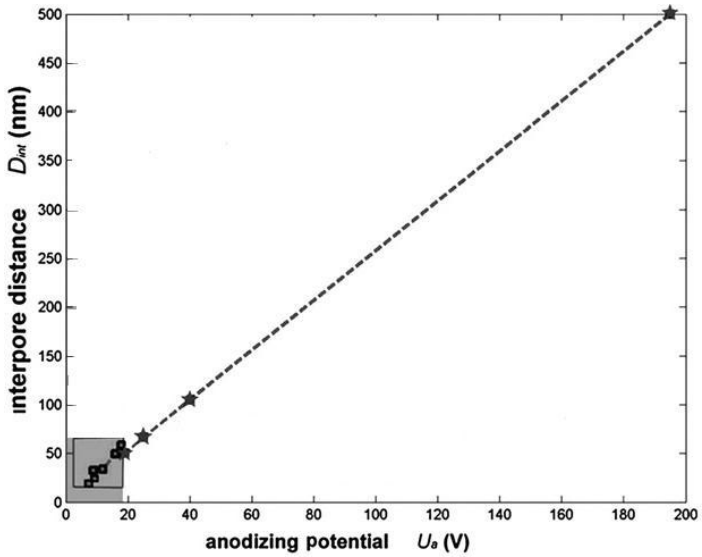

Figure 23. Relationship of the interpore distance and the anodizing potential. [73]

Here, AAO was fabricated by anodizing an Al film deposited on top of SiO_2. [77] A 50 nm thick Ti layer was used as an adhesion layer. A two step anodization process was performed in order to grow pores vertically to the substrate. [78] Figure 24 describes the process schematically. SEM images follow in figure 25. First, the Al thin film is anodized in 0.3 M oxalic acid for 5 minutes at room temperature under a constant voltage of 40 V. Oxidized aluminum was etched in an aqueous mixture of phosphoric acid (5 wt %) and chromic acid (1.8 wt %) at room temperature for 10 minutes. The Al film was anodized in 0.3 M oxalic acid for 5 minutes at room temperature under the constant voltage

of 40 V followed by pore widening in 0.3 M NaOH. In pore widening process, the etching rate of the remaining layer called the barrier layer between the substrate and the pore is proportional to the etching time. After etching in NaOH for 30 seconds, pores become through-holes, being ready for the deposition. After Ni was deposited through the AAO using e-beam evaporation, the AAO template was removed by etching in NaOH, leaving 40 nm diameter Ni nanostructures on the substrate as shown in Figure 26.

Figure 24. Fabrication of Ni nanodots using AAO template

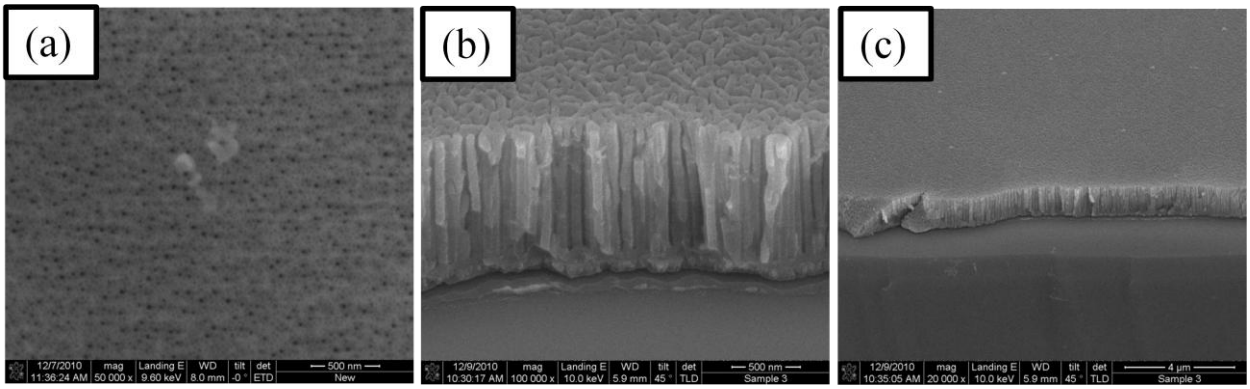

Figure 25. (a) SEM images of top view of AAO.

(b) and (c) (45° tilted) Cross sectional view of AAO.

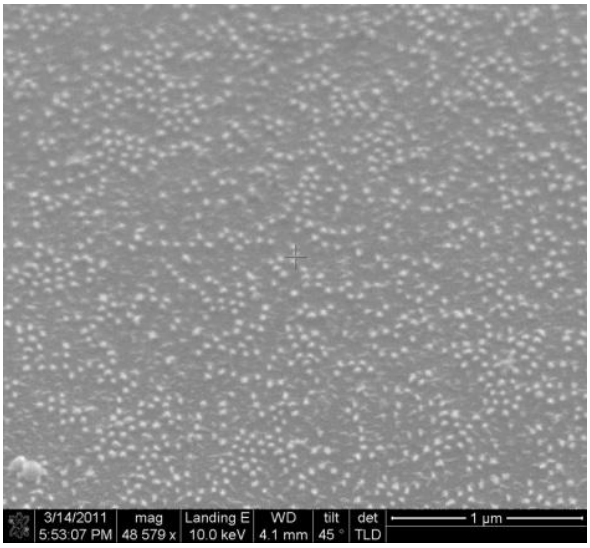

Figure 26. (45° tilted) SEM image of cross sectional view of 40 nm diameter Ni nanodots

In terms of physical size control of the nanostructures using an AAO template, we achieved pore diameters ranging from 20 nm to 100 nm by varying key parameters such as the voltage applied and the acids used in the aluminum anodization process. Anodizing an aluminum thin film in 20 wt % sulfuric acid while applying 18.7 Volts resulted in 20 nm pore diameter as indicated in Figure 27 (a). Figure 27 (b) shows 100 nm pore diameters in the AAO which was obtained by applying 195 Volts in 10 wt % phosphoric acid.

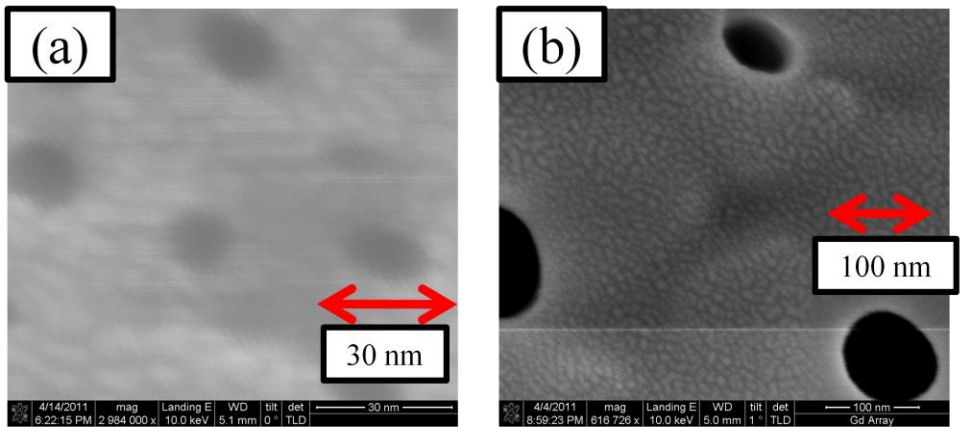

Figure 27. 20 (a) and 100 nm (b) pore diameter in AAO

2.2. Di-block Copolymer

Nanostructure fabrication using di-block copolymer (DBC) templates are an alternative to the AAO method in that DBC template works better for smaller feature size (5-50 nm). [54, 55, 79-82] Here, as with the AAO, the goal was to fabricate a large array of nanoscale multiferroic structures rather than individual structures. A DBC consists of two alternating monomer units which self-assembles into highly ordered periodic nanodomains of one monomer inside a matrix of the second monomer. [83] The shapes of the periodic nanodomain include lamellar, cylindrical and spherical patterns depending on the chemical composition of DBSs. Of these morphologies, DBC thin films with cylindrical domain structures oriented normal to the substrate can be used as a nanotemplate after selectively removing these cylindrical domains.

Ni nanostructures were successfully fabricated using a DBC made from poly(styrene-block- methyl methacrylate) (PS-b-PMMA) copolymer. [54, 80, 83-85] The diameter of the pores was ~25 nm and the interpore distance was ~40 nm. The PMMA domain was removed selectively by UV exposure. After Ni deposition using e-beam evaporation, the template was removed by etching in a piranha solution at 130 ℃. Figure

28 describes the fabrication process schematically. The diameter of the Ni nanodots was 20 nm as shown in figure 29.

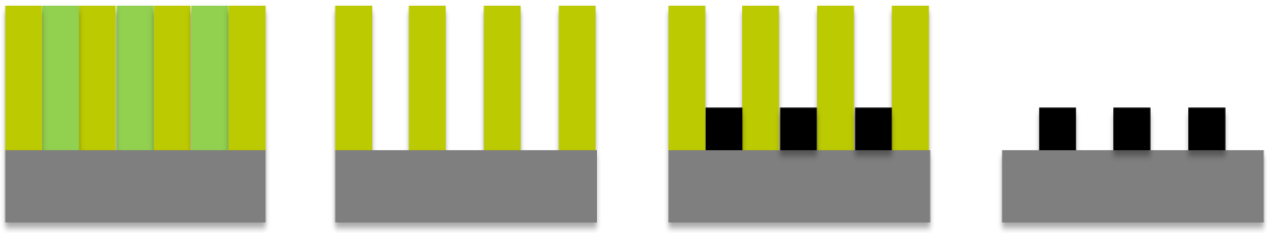

domain separation selective removal Ni deposition template etching

Figure 28. Fabrication of Ni nanodots using DBC template

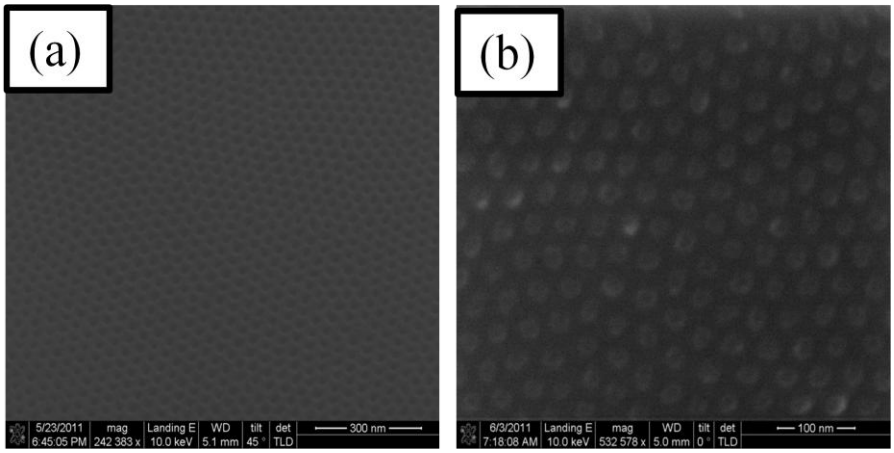

Figure 29. (a) (45° tilted) Cross sectional view of DBC nanotemplate.

(b) Top view of Ni nanodots. (20 nm diameter, 10 nm thick)

2.3. Chemical Synthesis

While templates methods were successful in fabricating single domain magnetic nanoparticles, smaller sizes were required to observe superparamagnetic properties at room temperature. In order to achieve this, chemical synthesis was employed due to its ability to fabricate nanoparticles as small as a few nanometers. 16 nm diameter Ni nanocrystals are superparamagnetic at room temperature and were synthesized via thermal decomposition of Ni(acac) in the presence of oleyamine (7 ml), oleic acid (2 mmol), and triocylphosphine (2 mmol). [86] The solution was stirred at room temperature for 20 minutes under gentle Ar flow before heating first to 130 C for 30 min, and then to 240 C (reflux) for 30 min. The solution was then cooled, and the particles were precipitated in ethanol and centrifuged. Two further washings were done with ethanol and hexane followed by centrifugation to remove any unbound ligand. Figure 30 shows TEM images of the as-synthesized Ni nanocrystals indicating that they are both spherical and monodispersed in size.

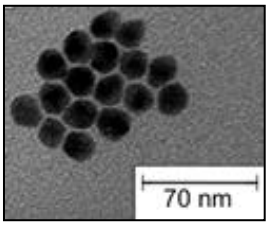

Figure 30. TEM image of several as-synthesized Ni nanocrystals.

3. Magnetoelectric Effect in Superparamagnetic Nanoparticles

Although there are a handful of publications on the magnetoelectric effect in magnetic thin films and single domain nanostructures during the last five years, reports on the magnetoelectric effect in superparamagnetic nanoelements were absent. In chapter 3, we first demonstrate the control of magnetization in 16 nm diameter Ni nanoparticles by using electric field induced strain from (011) oriented PMN-PT. In addition to this discovery, the blocking temperature of the particles was increased by 40 K and the amount of the blocking temperature change showed a good match with the increase of 46 K that was calculated from Arrhenius-Néel equation combined with magnetoelastic anisotropy.

3.1. Background

Magnetic Random Access Memory (MRAM) is attracting considerable attention as a potential candidate for future non-volatile memory. The two major challenges facing engineers today are overcoming the thermal instability associated with nanoscale magnetic elements and reducing the write energy to encode a bit of information. [87-90] As bit density increases (bit size decreases), superparamagnetism comes into play, resulting in

loss of information. Efforts have been made to overcome this effect by adding magnetic anisotropy to ferromagnetic materials using exchange-bias with antiferromagnetic materials. [56, 57] To address the problem of high write energies, researchers have begun studying heat-assisted magnetic memory [91, 92] and magnetoelectric memory [31, 32, 93-95] to modulate coercive field and thus reduce write energies. While these methods show promise, they do not address the more fundamental problem of controlling superparamagnetism. If an approach to modulate superparamagnetism is found, it would represent a major scientific advancement impacting a number of topical areas including MRAM. Here we report experimental results demonstrating that electric-field-induced anisotropy in a magnetoelectric nanoscale magnetic system. This modulation of the superparamagnetic transition is achieved via an electric-field-induced strain in a magnetoelectric composite composed of Ni nanocrystals mechanically coupled to a (011) oriented PMN-PT single crystal substrate. The system is capable of electrically switching between a superparamagnetic state and a single-domain ferromagnetic state at constant temperature.

3.2. Fabrication

The magnetoelectric composites used in this work were composed of ferromagnetic 16 nm diameter Ni nanocrystals mechanically coupled to (011) [Pb(Mg1/3Nb2/3)O3](1-x)-[PbTiO3]x (PMN-PT, x≈0.32) ferroelectric single crystal substrates. The Ni nanocrystals were synthesized via thermal decomposition of Ni(acac) in the presence of oleyamine, oleic acid, and triocylphosphine. [86] Figure 30 shows TEM images of the as-synthesized Ni nanocrystals. Magnetoelectric composites were produced by slowly evaporating a dilute solution of Ni nanocrystals dissolved in hexane onto an unpoled PMN-PT substrate with a thin titanium adhesion layer in an Ar atmosphere. [96] An SEM image of the particles deposited onto the substrate is shown in figure 31, demonstrating that a homogeneous sub-monolayer distribution is produced. The organic ligands on the particles were subsequently removed in an inert atmosphere using a two minute argon plasma etch. Without breaking vacuum, a 30 nm thick Pt layer was deposited onto the PMN-PT substrate to fully encase the Ni particles and protect them from oxidation. The Pt layer also provides a load transfer path from the PMN-PT substrate to the Ni nanocrystals. A schematic of the complete magnetoelectric architecture is shown in figure 32.

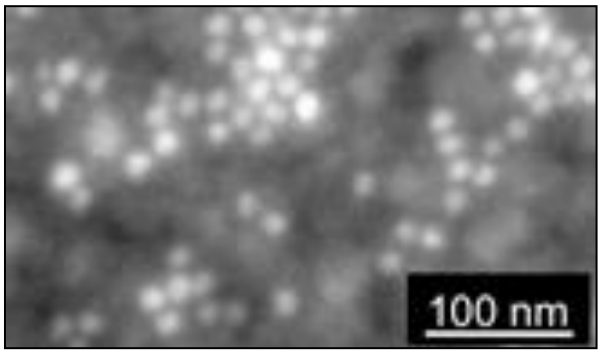

Figure 31. A SEM micrograph of the nanocrystals after deposition onto the piezoelectric substrate. Sub-monolayer coverage of non-agglomerated nanocrystals is observed.

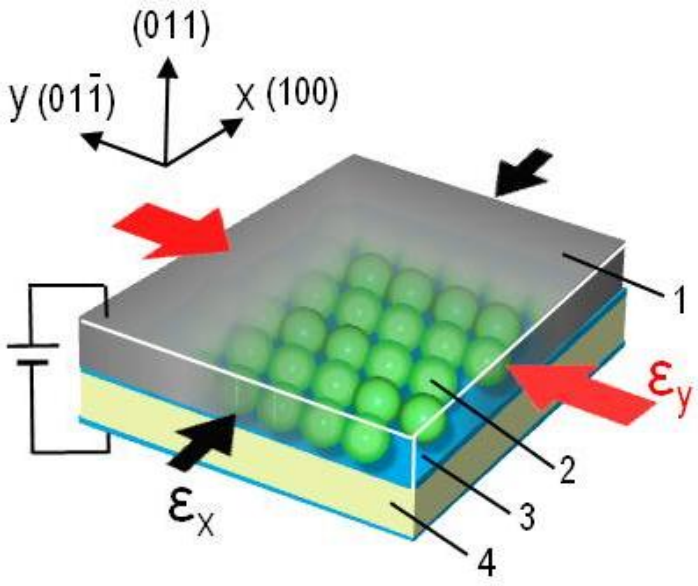

Figure 32. A schematic representation of the full device. 1: 30 nm thickness Pt layer (drawn partially transparent for clarity). 2: 16 nm diameter Ni nanocrystal. 3: 10 nm thick Ti electrodes evaporated on the top and bottom of the PMN-PT. 4: 500 μm thick (011) oriented PMN-PT single crystal substrate. Arrows indicate the direction of induced anisotropic strain.

3.3. Experiments and Results

Magnetic measurements on the magnetoelectric sample were performed before and after poling the PMN-PT substrate at room temperature. Figure 33 shows the anisotropic in-plane (x-y plane) strains generated as a function of applied electric field measured using a bi-directional strain gauge attached to the sample. In the unpoled state, the Ni particles in the magnetoelectric sample are subjected to negligible strains ($\varepsilon_x = \varepsilon_y = 0$). During poling (i.e. E = 0.4 MV/m), compressive strains up to $\varepsilon_x = -1200$ με and $\varepsilon_y = -800$ με are produced. Upon removal of the electric field, large anisotropic compressive strains of $\varepsilon_x = -300$ με and $\varepsilon_y = -1000$ με are present in the poled state. Since Ni has a negative magnetostriction coefficient, any induced magnetoelastic anisotropy causes the magnetic

dipoles in the single domain Ni nanocrystals to align along the dominant compressive strain direction (which corresponds to the deeper energy well). [35, 97] For the poled state, the larger anisotropic strain along the y-axis direction produces this deeper energy well.

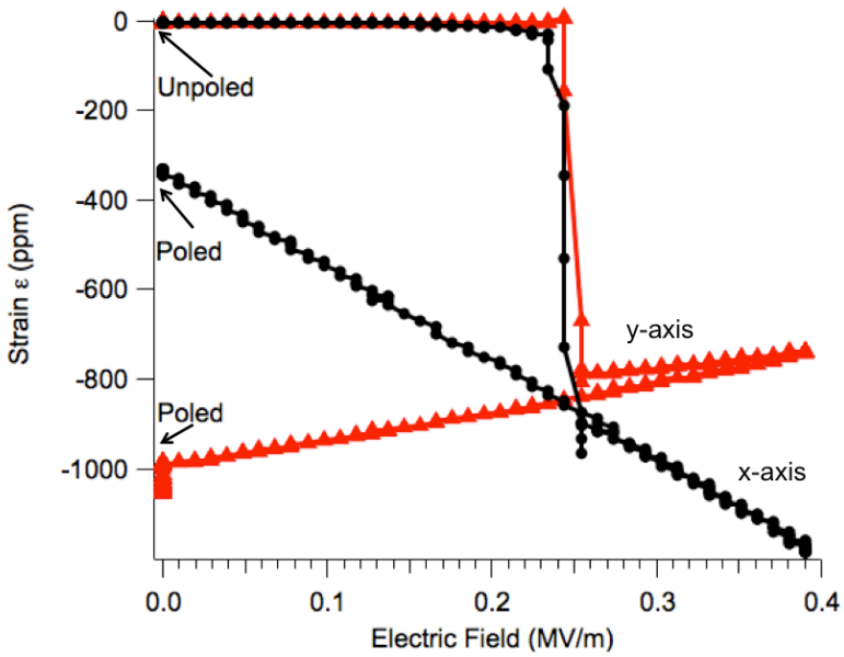

Figure 33. The strain induced in PMN-PT via an electric field applied along the (011) direction. Red triangles indicate strain along the y-axis, black circles along the x-axis.

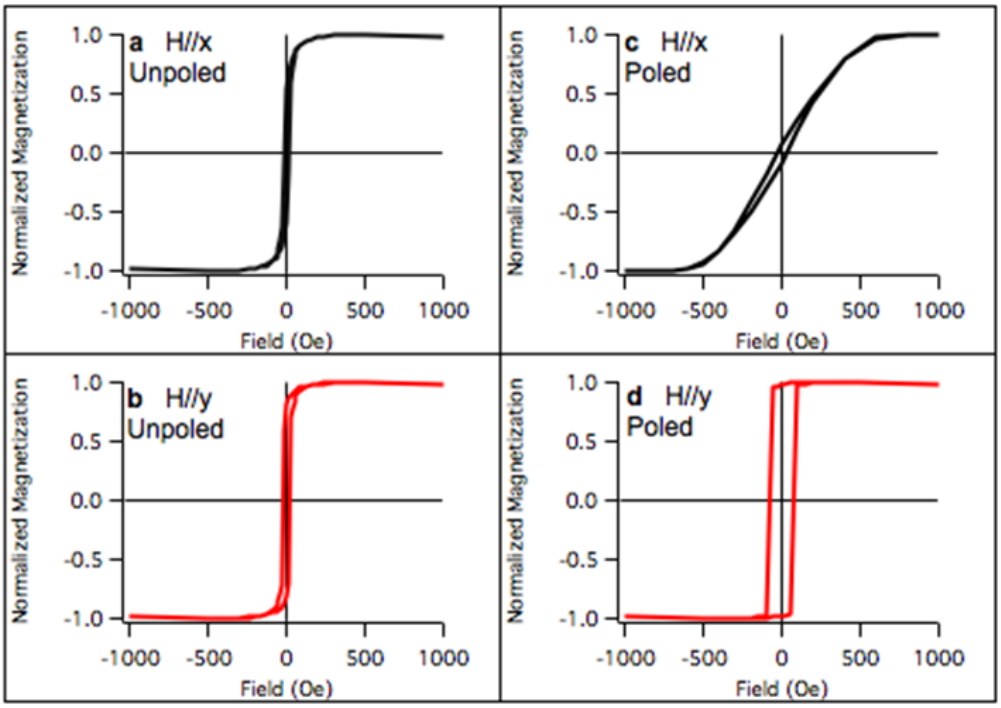

Figure 34. Magnetic hysteresis curves obtained on nickel nanocrystals embedded in Pt thin film on top of (011) PMN-PT at 298 K. Parts a, b show data measured with the magnetic field applied parallel to the x- and y-axes, respectively on the unpoled sample. Parts c, d show data measured with the magnetic field applied parallel to the x- and y-axes, respectively on the poled sample.

Figure 34 (a) and 34 (b) show magnetic moment (M) measurements at room temperature as a function of the applied magnetic field (H) for the unpoled (i.e. $\varepsilon_x = \varepsilon_y = 0$) magnetoelectric composites measured in x- and y-directions, respectively. Measurements were conducted using a superconducting quantum interference device (SQUID, Quantum Design, MPMS XL-5). Similar, small coercive fields, $H_c < 20$ Oe, are observed in both directions indicating that the sample is both magnetically isotropic in-plane and dominantly superparamagnetic. The small anisotropies observed are attributed to small variations in the spatial distribution of nanocrystals produced during the evaporative deposition process used to manufacture the magnetoelectric composite. Figure 34 (c) and 34 (d) show similar magnetic measurements on the poled ($\varepsilon_x = -300$ με, $\varepsilon_y = -1000$ με) magnetoelectric composite. The data in figure 34 (c) shows a hard magnetic axis is created parallel to the x-direction for the poled sample with a magnetic anisotropy (H_a) of 600 Oe. The ratio of the remanent magnetization (M_r) to the saturation magnetization (M_s) is very low, suggesting that domains tend to orient in an off-axis direction. In contrast, figure 34 (d) shows a magnetic easy axis is created along the y-direction for the poled sample. In this direction, M_r is approximately equal to M_s, indicating that the sample consists of essentially single domain Ni nanocrystals that are aligned along the y-axis. Furthermore, H_c=80 Oe

measured along this direction confirms a deeper potential well for spin alignment is present in the y-direction after application of an electric field.

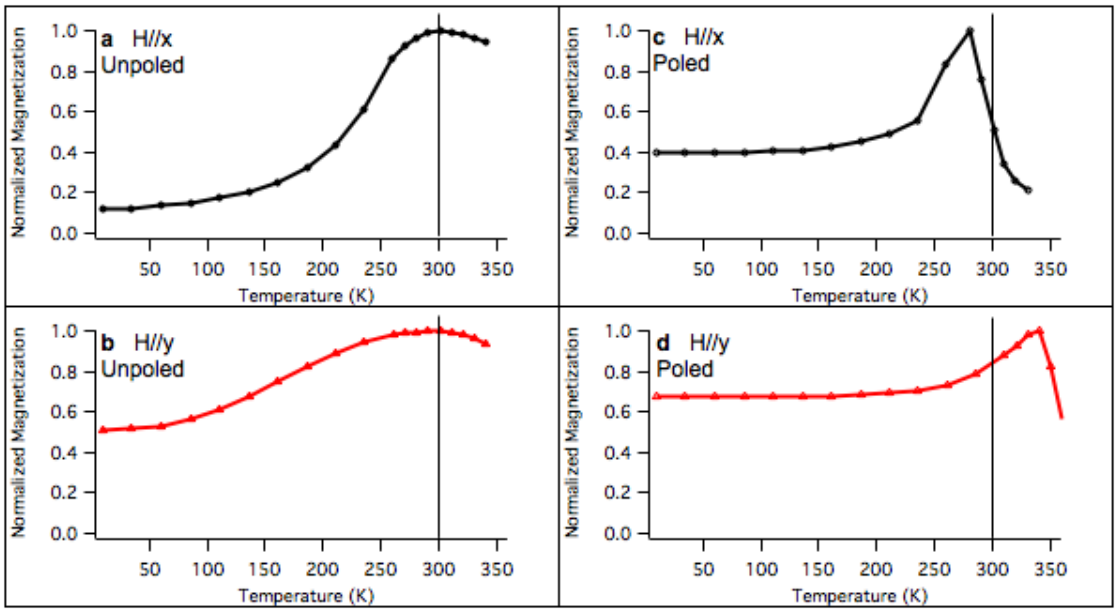

Figure 35. Zero field cooled (ZFC) magnetization curves as a function of temperature for Ni nanocrystals embedded in Pt on (011) PMN-PT before and after electrical poling. All data is normalized to 1 at the peak magnetization. Parts a and b show data on the unpoled sample, measured in the x- and y-directions, respectively. Parts c and d show data on the

poled sample, again measured in x- and y-directions, respectively. All curves were measured using a 50 Oe applied field.

Figure 35 (a) and 35 (b) show normalized magnetic moments as a function of temperatures for the unpoled magnetoelectric sample. Samples were initially cooled to 10 K in the absence of a magnetic field (zero field cooling, ZFC) followed by measurement of the magnetic moment as a function of temperature in a 50 Oe applied field. The temperature corresponding to the highest magnetic moment is typically defined as the blocking temperature (T_B), above which magnetic dipoles begin to lose their directionality due to thermal randomization and the sample becomes superparamagnetic.[98] There are some small differences in the data measured in the x- and y-directions, which are attributed to the evaporative deposition process, as discussed previously. Nonetheless, similar blocking temperatures of ~300 K are found in the unpoled state in both directions. By contrast, figure 35 (c) and 35 (d) show ZFC curves for the poled magnetoelectric sample measured along the x- and y-directions, respectively. The data measurements in the x-direction (hard axis) shows a peak at 280 K, which represents a decrease of 20 K compared to the peak observed in the unpoled samples (figure 35 (a) and 35 (c)). More dramatically,

for the y-direction (easy-axis) the peak of the magnetization curve (or T_B) increases to 340 K, or a change of 40 K when compared to the peak in the unpoled samples.

3.4. Discussion

The shifts in the maximum of the ZFC curves can be explained by considering how the potential landscape for spin alignment is changed in an anisotropically strained sample. In the unpoled sample, the magnitude of the barrier for spin flip is on the order of the available thermal energy at room temperature and so the spins begin to hop between magnetic easy axes as the blocking temperature of 300 K is approached. When the sample is anisotropically strained by the PMN-PT substrate, however, the potential well for spin alignment in the y-direction is deepened. It thus requires significantly more thermal energy for the spins to hop out of this deeper well, and so the blocking temperature shifts to well above room temperature (340 K) after electric poling. In the x-direction, the blocking temperature appears to decrease, but this is not a true blocking temperature, as the fall-off in magnetization at 280 K is not thermal randomization of magnetic moments, but rather magnetization transfer from the x-direction to the y-direction as the system obtains sufficient thermal energy to free the spins from the metastable potential minima where they

were trapped. Because spins are directionally transferring from a high energy configuration to a lower energy configuration, the process occurs at a lower temperature than the thermal randomization observed in the unpoled sample. The true blocking temperatures in the unpoled and poled system are thus 300 K and 340 K respectively.

The above conclusions can be confirmed using the Arrhenius-Néel equation, $\frac{1}{\tau} = \frac{1}{\tau_0} e^{\frac{-KV}{k_B T}}$, where τ is the magnetization switching time, K is total anisotropy energy density, V is particle volume, k_B is Boltzman's constant, T is the temperature, and $\frac{1}{\tau_0}$ is the attempt frequency. [40, 42, 43] Using $\frac{1}{\tau_0} = 10^9$/second and τ = 100 seconds produces the familiar $KV = 25k_BT$ relation. [44, 99] For this system, the electric-field-induced change in the magnetoelastic anisotropy is approximated by $\frac{3}{2}\lambda Y \Delta\varepsilon_a$, where λ = -34 με is the Ni magnetostrictive constant, Y = 213.7 GPa is the Ni Young's modulus and $\Delta\varepsilon_a$ = –700 με is the residual strain induced in the Ni nanocrystal after electric poling (see figure 33). [35, 97] Incorporating this anisotropy term into the Arrhunius-Néel equation produces $\frac{3}{2}\lambda Y \Delta\varepsilon_a = 25k_B\Delta T_B$, which provides an estimate of the blocking temperature change ΔT_B

that should result from the additional magnetoelastic energy added during electric poling. The calculated value of 46 Kelvin is in good agreement with the measured value of ~ 40 K. Moreover, using the Arrhenius-Néel equation and our estimate for the electric-field-induced change in the magnetoelastic anisotropy, one can calculate the strain needed to convert our 16 nm superparamagnetic Ni nanoparticles into ferromagnetic bits with a thermal stability of τ = 10 years at room temperature (which is considered standard). [100] To achieve this stability only a modest increase in strain, from $\Delta\varepsilon_a$ = -700 to $\Delta\varepsilon_a$ = -980 $\mu\varepsilon$ is needed; this increase is easily achievable using other piezoelectric materials currently available today. [30]

While increasing the magnetic anisotropy is crucial to stabilizing magnetic bits, increasing anisotropy (and thus bit stability) unfortunately leads to increases in write energy. However, for the magnetoelectric system studied in this work, the magnetic anisotropy can be electrically modulated, thus reducing the required write energy for a bit of information. As shown in figure 34 (d), the coercive field of the poled sample is H_c = 80 Oe. Examination of figure 33 indicates that application of a 0.24 MV/m electric field reduces the magnetoelectric anisotropy to zero (i.e. $\varepsilon_x = \varepsilon_y$ or $\Delta\varepsilon_a$=0), returning the sample to near the superparamanetic state (H_c<20 Oe), as observed in the unpoled samples (figure 34 (a) and 34 (b)). This approach provides an electrical mechanism to dramatically decrease the

magnetic energy required to write a bit of information. In this way, magnetoelectric coupling in small magnetic particles can be used to both increase the blocking temperature, and decrease magnetic write energies, a combination that is simply not possible in conventional magnetic systems.

3.5 Summary

By applying electric-field-induced strain to the ferromagnetic nanocrystals, we demonstrate a shift in the blocking temperature of approximately 40 degrees Kelvin. More importantly, this shift is centered directly over room temperature, so that the sample is superparamagnetic (no permanent magnetic moment) at room temperature before application of an electric field, and is a strong single-domain ferromagnetic at room temperature after application of an electric field. Magnetoelectric control of the blocking temperature may provide exciting opportunities to explore new types of memory devices, not only using smaller bit size by superparamagnetic modulation but also using less write energy by taking advantage of an electric field to reduce H_c.

4. Correlation between Magnetodielectric Coefficient and Magnetic Anisotropy

Research on the magnetoelectric effect has attracted a great interest due to its unique coupling between an electric field and a magnetic field with a trend towards to device miniaturization. Nowadays the focus of the research is on the bulk laminate magnetoelectric composites since the coupling mechanism between polarization and magnetization in single phase magnetoelectric materials is still lacking, making it difficult to find a single phase magnetoelectric materials with strong magnetoelectric coupling. [11] Recently, we discovered that the maximum values of magnetodielectric coefficient of γ–Fe_2O_3 correlates with maximum values of the magnetic anisotropy at a certain temperature. The discovery suggests that the magnetic anisotropy may play a significant role in single phase magnetoelectric coupling. In chapter 4, a brief literature review will be presented, followed by the experimental procedures and a discussion which will focus on the correlation between the max value of MD % and the magnetic anisotropy.

4.1. Background

Nanoscale γ–Fe_2O_3 has attracted a great deal of interest among iron oxide polymorphs due to their extensive and promising applications such as a magnetic information storage or medical diagnosis. However, properties occurring in the nanosized particles below a certain size have limited the use of the particles. [101] The spin canting phenomena is one of the more important factors resulting from magnetic nanoparticles and strongly influences the magnetic moments when an external magnetic field is applied. Recently, we experimentally discovered that the maximum values of the magnetodielectric coefficient of γ–Fe_2O_3 correlates with the maximum values of magnetic anisotropy at a certain temperature. This is believed to be related to the spin canting phenomenon. Therefore, the goal of this study is to advance the understanding of the relationship between the magnetodielectric constant and the magnetic anisotropy.

In 2003, Kimura et al [62] demonstrated that the magnetodielectric constant (MD %), defined as $\frac{\varepsilon(H)-\varepsilon(0)}{\varepsilon(0)} \times 100,\ (\varepsilon = dielectric\ constant)$ in $BiMnO_3$ increases with increasing temperature and showed the maximum occurs around the magnetic transition temperature. However, recently, experimental reports and first principle calculations

report that the maximum values in MD % are found at temperatures far below magnetic transition temperatures. [102-105] Bonaedy [102, 104] and Koo [103] performed an extensive study on γ–Fe_2O_3 from 2007 to 2008, in which they reported that the MD effect in γ–Fe_2O_3 is maximized around 200 K which is far below the transition temperature of 948 K. While interesting, a clear explanation for this maximum has not been provided. In this section we measured the magnetodielectric coefficients and magnetic anisotropy of γ- Fe_2O_3 nano-composites.

Strictly speaking, the relatively high room temperature conductivity of γ- Fe_2O_3 (~0.25 Ω cm) suggests that it is not a conventional magnetoelectric. [64] Hence, the magnetodielectric properties measured in this material are attributed to the materials' magnetoresistive response rather than polarization changes. It was first pioneered and predicted by Catalan [61] that the magnetodielectric effect can occur through a combination of the Maxwell–Wagner effect and magnetoresistance, which are not directly related to the magnetoelectric coupling. Testing this magnetoelectric coupling requires the observation of a change in the electrical polarization due to a magnetic field or a change in magnetization due to an electric field. However, since many possible single phase magnetoelectrics are poor insulators, they cannot sustain an electric field large enough to

align electrical polarization, which therefore makes this test difficult to perform. [61] An alternative method to confirm the magnetoelectric coupling is to measure the dielectric constants as a function of a magnetic field and/or temperature.

Bonaedy et al [104] measured the dielectric constant of γ- Fe_2O_3 as a function of frequency from 10^2 to 10^6 Hz at 293 K. The dielectric constant strongly depended on both parameteres. Due to the strong dependences of non ferroelectric γ- Fe_2O_3 as well as its polycrystalline nature, the Maxwell-Wagner model was utilized. The Maxwell-Wagner two capacitor model has two capacitors in series that have R_G, C_G and R_{GB}, C_{GB}, respectively. (G : grain, GB : grain boundary, R : resistance, C : capacitance) The real and imaginary parts of the complaex dielectric constant in the Maxwell-Wagner two capacitor model can be written as

$$\varepsilon_1 = \frac{1}{C_0(R_G + R_{GB})} \frac{\tau_G + \tau_{GB} - \tau + w^2 \tau_G \tau_{GB} \tau}{1 + w^2 \tau^2}$$

$$\varepsilon_2 = \frac{1}{wC_0(R_G + R_{GB})} \frac{1 - w^2 \tau_G \tau_{GB} + w^2 \tau(\tau_G + \tau_{GB})}{1 + w^2 \tau^2} .$$ [61, 102, 104]

(w : ac frequency, τ_G : $R_G C_G$, τ_{GB} : $R_{GB} C_{GB}$, $\tau = (\tau_G R_{GB} + \tau_{GB} R_G)/(R_G + R_{GB})$, C_0 : capacitance of vacuum). At low and high frequencies, ε_1 can be approximated as

$$\varepsilon_1(w->0) = \frac{R_G^2 C_G + R_{GB}^2 C_{GB}}{C_0 (R_G + R_{GB})^2}$$

$$\varepsilon_1(w->\infty) = \frac{C_G C_{GB}}{C_0 (C_G + C_{GB})} \text{ . [104]}$$

This approximation indicates that the dielectric constant depends on the resistance of the grains and their grain boundaries, especially in the the low frequency case; at high frequencies only the capacitances of the grain and grain boundaries are considered. [104]

Due to the difference in work functions at the interface between an electrode and a dielectric material, the band theory diagram bends at the interface between the electrode and the dielectric material. [61] The resultant charge movement across the interface results in an interfacial layer between the electrode and the dielectric material with a different density of charges, leading to different resistivity than that of the core. [61] For a bad insulator, this causes a prominent drop in the applied electric field within single crystals that have large charge depleted interfacial layers as well as polycrystalline samples with grain boundaries as shown in figure 36. [61] The drop in the electric field produces a large

dielectric constant, proving that multiferroic materials with poor insulating capabilities can exhibit the magnetodielectric effect. [61]

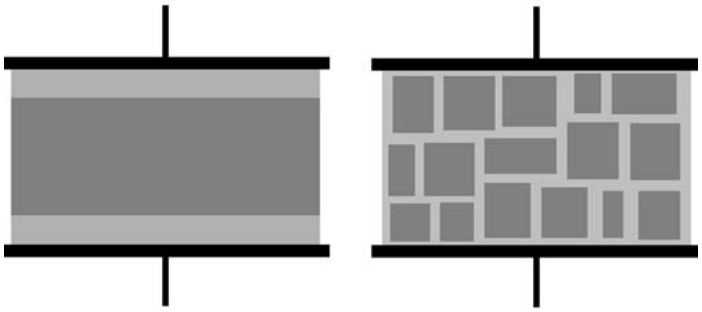

(a) (b)

Figure 36. Capacitor structures with Maxwell-Wagner behavior. (a) Single crystal with charge-depleted interfacial layers and (b) ceramic with charge-depleted grain boundaries [61] For a ceramic, interfacial polarization takes place at the interface of grains and grain boundaries.

The Maxwell-Wagner capacitor model has been used to explain the dielectric properties of magnetoresistive materials in numorous works since 2006. [64, 103, 104]

4.2. Fabrication

Polycrystalline γ- Fe_2O_3 nano particles of size ~ 10 nm (Alpha Aesar, USA) were mixed with epoxy resin (Spurr resin, Polysciences Inc.) by 25% particle volume content (i.e. 60% by weight). The liquid resin containing nanoparticles was mixed under constant ultra-sonication and UV radiation in order to disperse the nanoparticles. It was noted that nanoparticles are not completely dispersed in the resin due to the opaque appearance of the sample. Curing was performed at 70 ^{o}C for 12 hours in vacuum. The sample was then cut into a plate-shape and silver paste was applied to the top and bottom of the sample to be used as electrodes. A picture and schematic of the sample is shown in figure 37.

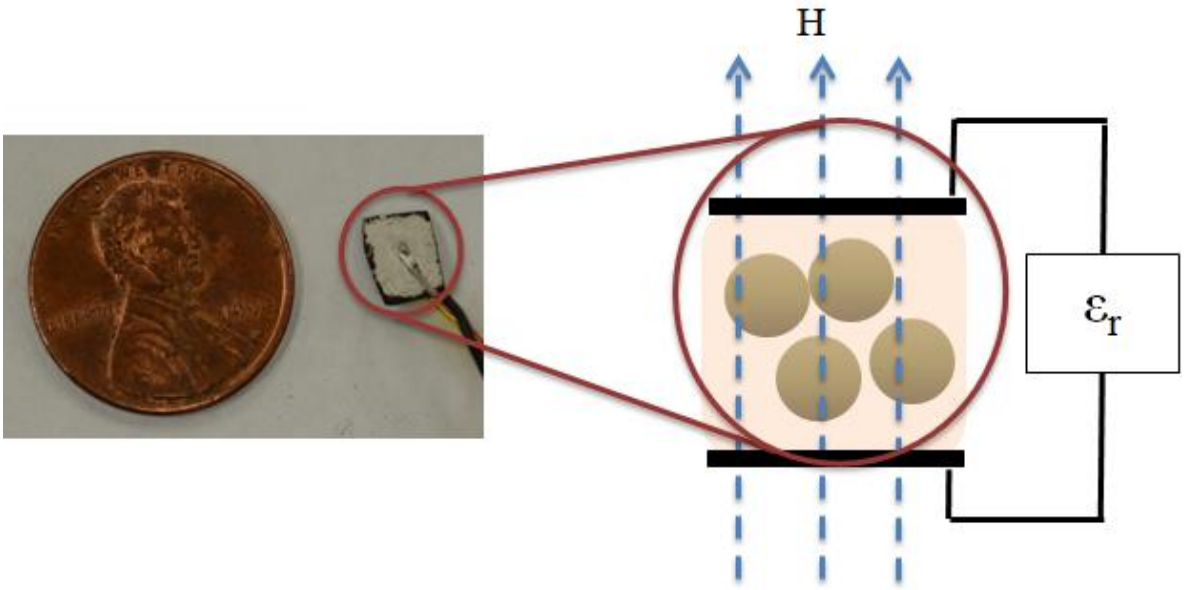

Figure 37. 25% volume fraction of γ- Fe_2O_3 (~ 10 nm) embedded in epoxy resin and the schematic measurement setup for dielectric constant

4.3. Experiments and Results

The samples dielectric constant and resistance were measured using a standard two probe method with an HP 4274A multi frequency (0-100 kHz) LCR meter at different DC magnetic field biases ranging from 0 to 1.5 T. The magnetic field strength was monitored by a Gauss meter (FW Bell 6010). Figure 38 shows an experimental setup for measuring the dielectric constant while a magnetic field was applied using an electromagnet.

Magnetization measurements at different temperatures along with a Zero Field Cooling study at 50 Oe were also measured using a SQUID.

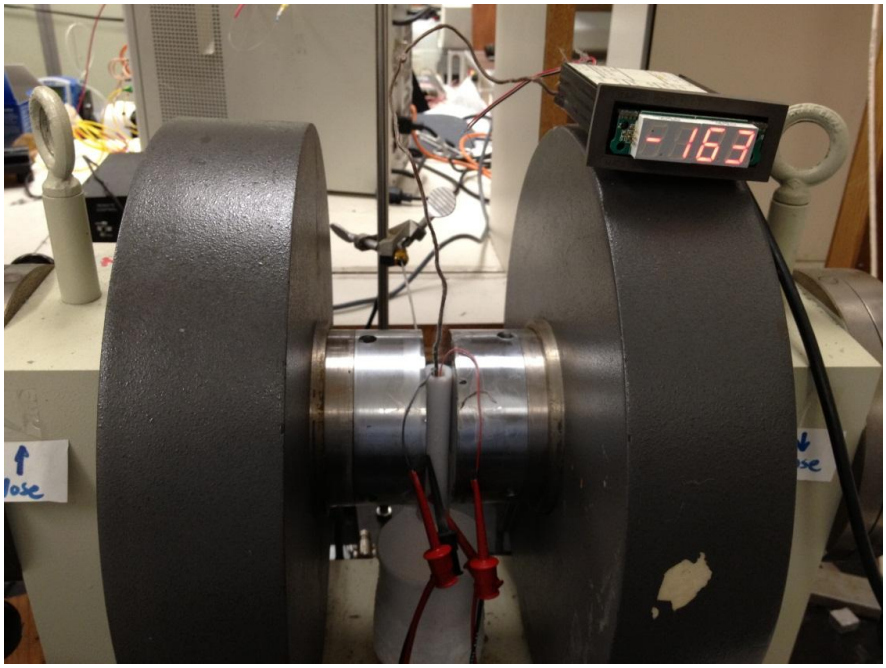

Figure 38. Sample loading setup. Sample is inserted into a Teflon holder. Magnetic field is applied using electromagnets sandwiching the holder.

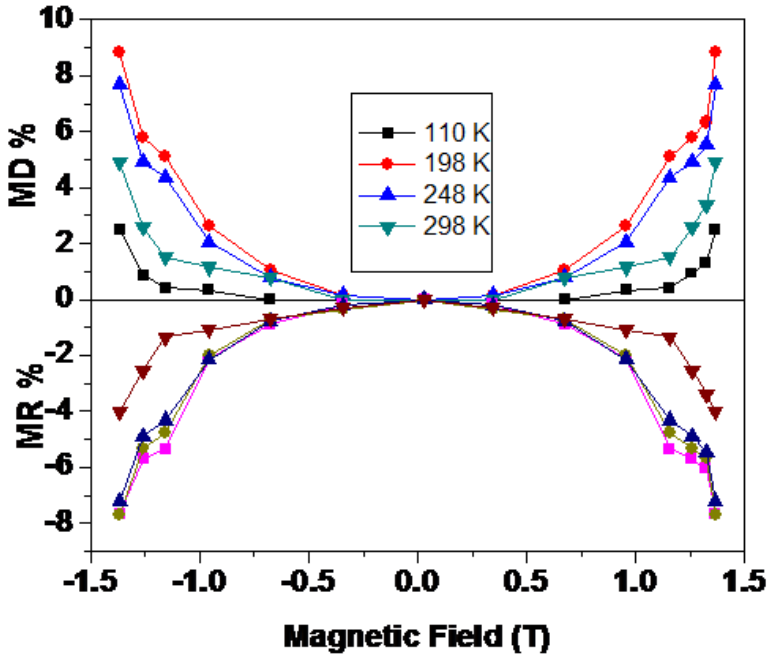

Figure 39. Magnetodielectric coefficient (MD %) and magnetoresistance (MR %) of the nanocomposite measured at 100 kHz and at different temperatures and fields

Figure 39 shows the experimental data for the composite's magnetodielectric (MD) constant and magnetoresistance (MR) as a function of magnetic field bias for four different temperatures, each measured at 100 kHz frequency. The MR % is defined as $\frac{R(H)-R(0)}{R(0)} \times 100, (R = resistance)$. Figure 39 indicates an increasing dielectric response and

decreasing resistance as magnetic field increases, i.e. a positive magnetodielectric effect. Furthermore, the results indicate that as temperature increases, the MD % increases followed by a decrease above 198 K while MR % shows relatively little changes as a function of temperature with the exception of 298 K.

The magnetoresistance and the magnetodielectric properties in γ–Fe_2O_3 have been observed and explained by spin-dependent tunneling through networks of continuous groups of atoms, that is caused by the relative alignment of their magnetizations. [101] The relative spin arrangement controls the probability of tunneling; a more aligned configuration favors tunneling with a reduction in resistance (increase in dielectric property), and vice versa. The relationship between resistance and spin alignment can be understood with regard to electron scattering depending on spin alignment. When an electron is scattered, the electrical resistance will be increased. In a group of magnetic nanoparticles, the alignment of the adjacent spins determines the probabilitiy of electron scattering. If a majority of spins align in the same direction due to the high magnetic field which can contribute to the spin alignment, the chance of electron scattering will be reduced. If the spins are randomly aligned, electrons will need an additional energy for them to change their spin state from an up-spin state to a down-spin state, and vice versa for

them to be tunneled through spins. From an applicational standpoint, the spin-dependent tunneling governing magnetoresistance provides a basis for the giant magnetoresistance.

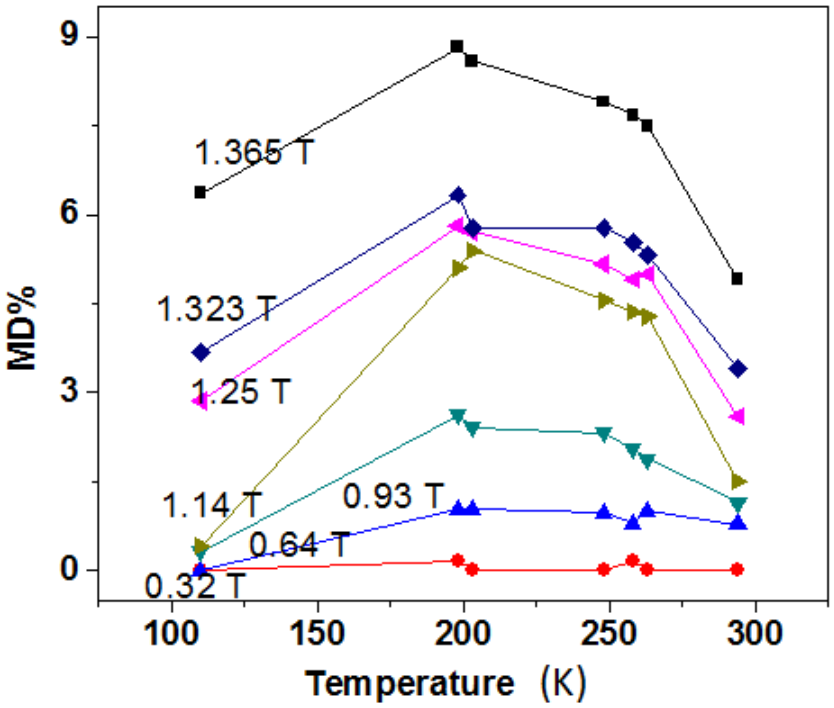

Figure 40. Magnetodielectric coefficient under different magnetic fields

at diffeent temperatures

Figure 40 shows the MD % shown in figure 39 as a function of temperature at selected magnetic fields. The experimental data indicates that the MD % increases from 110 K to ~ 200 K and then decreases from ~ 200 K to 298 K for all magnetic fields tested. The maxima reached at ~ 200 K is approximately 9 % at ~1.4 T which is substantially larger than either the ~2.5 % measured at 110 K or the ~5 % at 298 K. Experimental data for γ- Fe_2O_3 in the literature also reports a maximum MD % at ~200 K even though its T_c ~ 948 K. [103, 104] For example, Bonaedy et al reported a maximum at 1 Tesla and 200 K for 25 nm of γ- Fe_2O_3 particles and a maximum at 6 Tesla and 200 K for $BaTiO_3$/γ- Fe_2O_3 [103, 104]. However, Lawes et al. [64] reported a maximum at 300 K for 5.5 nm γ- Fe_2O_3 nanoparticles embedded in an insulating matrix.

The magnetodielectric effect depends on a number of factors including the Maxwell-Wagner capacitance effect due to magneto-capacitance along the grain boundaries and magneto resistance within the grains. [64] Furthermore, magnetic domain reorientation within the grains (magneto-resistance) influences the resistance and thus their dependency on a magnetic field. While the previous observation combined with the relationship between electron scattering and magnetic field dependent spin alignment explains the MD % changes with magnetic field, they do not explain the presence of a maximum in MD % as a function of temperature. It is of significant relevance to estimate

the effect of temperature on MD %, since it is well known that the spin canting phenomenon critically depends on the temperature. This led us to measure the magnetic response from our sample at different temperatures to address the issue. [101] (see figure 41)

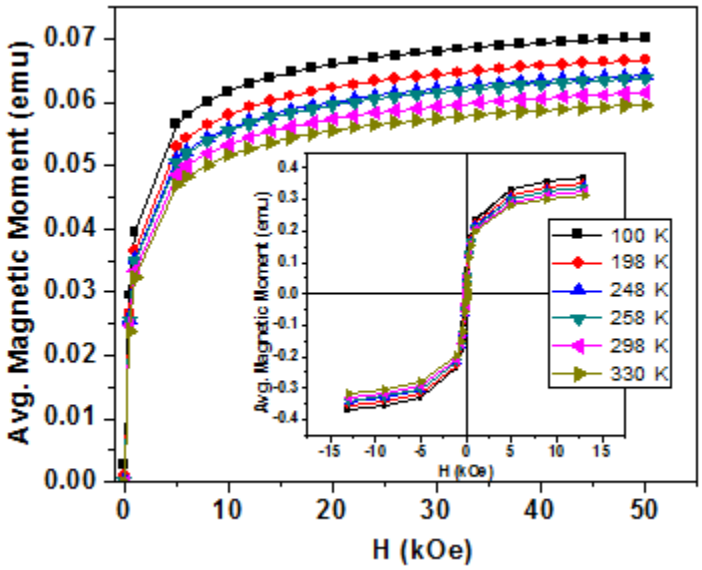

Figure 41. M-H curves for the nanocomposite

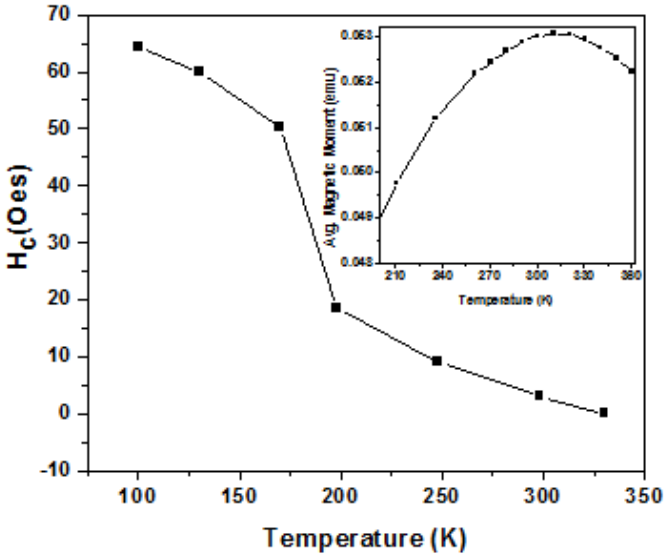

Figure 42. Variation of coercivity with temperature. The inset shows the ZFC curve of the composite representing T_B at ~330 K

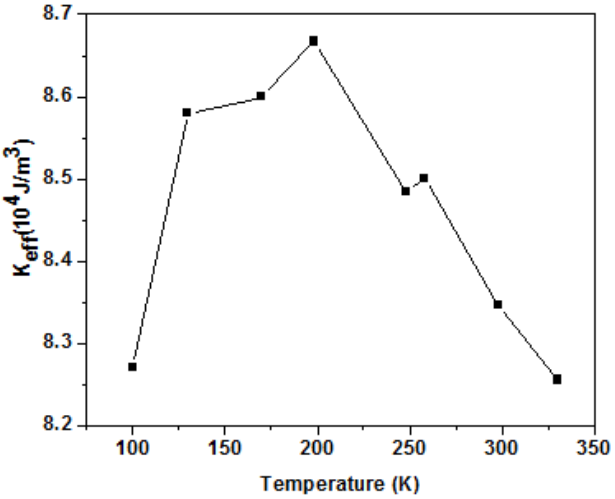

Figure 43. Temperature dependence of effective magnetic anisotropy

Figure 41 shows the samples magnetization as a function of field (from -5 Tesla to 5 Tesla) for the first quadrant at six different temperatures while the inset provides the full magnetization-magnetic field curves from -1.3 Tesla to 1.3 Tesla. This measurement is necessary in order to calculate the MD % using LATS method. Details about LATS model will follow the description of figure 42. As can be seen in the figure, the saturation magnetization decreases as temperature is increased monotonically due to increasing thermal agitation. At 298 K, the measured M_S of the composite is ~ 17 emu/g. Previously reports indicate that the M_S value of the bulk sample is larger than that of nanoparticles; Banerjee et al [106] : 79 emu/g for 35 nm γ- Fe_2O_3 nanoparticles, Wang et al [107] : 23.6 emu/g for 9 nm γ- Fe_2O_3 nanoparticles, Coey et al [108] : 59 emu/gm for 6.5 nm of γ- Fe_2O_3 nanoparticles, Leite et al [109] : 32 emu/g of M_S for 3 nm diameter γ- Fe_2O_3 nanoparticles. The differences in size dependent M_S values were attributed to the surface anisotropy present in the nanoparticles due to the increased surface to volume ratio. [106-109] Using a rule of mixtures approximation for the 25 % by volume (60 % by weight) composite, an analytical estimate of ~24 emu/g is predicted which is in relatively good

agreement with the measured values. Note the mass used above only takes into account the mass of γ- Fe_2O_3 nanoparticles.

Figure 42 shows the variation of coercive field (H_c) as a function of temperature and the inset shows the measured zero field cooling (ZFC) curves for the sample. H_c decreases with temperature and approaches zero near the blocking temperature, $T_B \sim 330$ K as indicated in the ZFC plot. It is an intuitive result considering the fact that the increasing thermal fluctuation reduces the required magnetic field necessary to align the magnetic moments, leading to the reduction of H_c. Below T_B, the sample is in the single domain magnetic state and the magnetic spins align in the easy axis defined by the effective magnetic anisotropy (K_E), while above T_B it is in the superparamagnetic state and the orientations of their magnetic moments shift from one easy axis to the other faster than the magnetization sampling rate. When the magnetic moments are in the superparamagnetic state, they rotate coherently. Thus the superparamagnetic state is essentially a thermally agitated single domain state. We can say that a certain sample is superparamagnetic when it is above its T_B.

The effective magnetic anisotropy K_E for the test sample is calculated, using the law of approach to saturation (LATS) and the experimental data shown in figure 41. K_E is the total magnetic anisotropy energy which includes shape, stress, crystalline and surface

magnetic anisotropy. Almost all nanocrystals have anisotropies that are dominated by shape or surface anisotropy and dipole coupling between nanocrystals. None of those effects are temperature dependant, however, therefore they do not contribute to the temperature dependant part of K_E. Therefore, only surface [110, 111] and magnetocrystalline anisotropy contribute to the effective magnetic anisotropy K_E. Since the surface anisotropy, whose origin is the lack of neighboring atoms at the surface, should not strongly depend on temperature, only the magnetocrystalline anisotropy contributes to the changes in K_E as a function of temperature. For polycrystalline nanoparticles, the LATS is

$$M(H) = M_S(1 - \frac{a}{H} - \frac{b}{H^2} - ...) + \chi_P H \qquad \text{(a)}$$

where M_s is the saturation magnetization and $\chi_p H$ is the paramagnetic term which is attributed to an increase in spontaneous magnetization due to the high external magnetic field. [112, 113] The origin of a/H is the strain field around dislocations and non mangetic imperfections in the materials; the origin of b/H^2 is the magnetic anisotropy. For magnetic materials with uniaxial anisotropy, the coefficient b is expressed by

$$b = \frac{4K_E^2}{15M_S^2}. \qquad \text{(b)}$$

Therefore, if we measure magnetization as a function of magnetic field (MH curve), we can get the value of b and M_s from equation (a), and ultimately, K_E from equation (b). [112, 113]

In the LATS model the magnetic anisotropy is calculated in the high field regimes ($H >> H_c$), since the high field regions represent the procession of magnetic moments against the magnetic anisotropy. [114] When considering the first order cubic anisotropy of random polycrystalline samples, the equation (a) is given as

$$M(H) = M_s\left[1 - \frac{8}{105}\frac{K_E^2}{\mu_o^2 M_s^2}\frac{1}{H^2}\right] + \kappa H. \quad [114]$$

Figure 43 shows the values of K_E as a function of temperatures for the Fe_2O_3 composites calculated using the LATS model and data from figure 41. As the temperature decreases from 330 K, K_E increases and passes through a maximum at ~200 K. Similarly a temperature dependent maximum for K_E has also been reported by Ranvah et al for a gallium substituted cobalt ferrite material [114], however they did not consider the correlation between K_E and MD %. In the following section, the temperature dependent spin canting phenomenon will be used to explain the correlation between K_E and MD %.

4.4. Discussion

It is well established that temperature affects the spin alignment of the magnetic nanoparticles. [101, 115-120] These temperature effects are more pronounced for nanoparticles exhibiting surface spin canting due to reduced average atomic coordination number which causes differing balance of exchange interactions at the surface. [121] Spin canting prevents surface spins from aligning with the applied magnetic field as shown in figure 44, resulting in a decrease of the saturation magnetization with a decrease in a particle size. [48, 101, 115-117, 119-123]

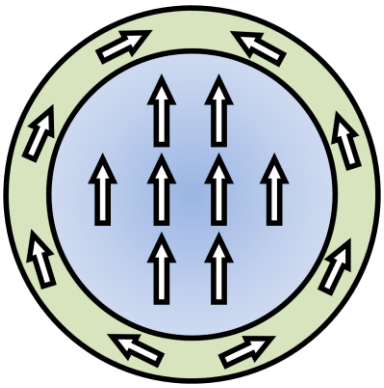

Figure 44. Schematic drawing of spin canting under the magnetic field applied upward direction. Spins close to the surface are canted due to reduction of atomic coordination number. [122]

It should be noted, however, that some previous researchers reported that spin canting is not limited as a surface phenomenon. [115, 119, 120] Unlike atomically ordered nanoparticles, structurally disordered nanoparticles may have defects, such as a vacancy or dislocation. A disordered nanoparticle might exhibit the spin canting in the internal atoms and it needs to be taken into account when describing the magnetic behavior of the magnetic nanoparticles. Morales et al [119] reported that the saturation magnetization of the ordered nanoparticles decreases linearly with reduction in a particle size, and that a steeper decrease was demonstrated in the disordered nanoparticles. This illustrates the

argument that spin canting within the internal structure played an important role in this phenomenon. While their statements are informative and important in understanding the phenomena, it is obvious that as the size of magnetic nanoparticles is reduced, the role of the surface spin canting becomes more significant in explaining the magnetic properties of nanoparticles due to an increase in surface to volume ratio.

Mössbauer spectroscopy is an experimental tool used to detect small changes in the energy levels of an atomic nucleus. This makes it a powerful method for studying spin canting and superparamagnetism since it enables one to quantify and qualify the degree of the phenomena. [101, 117, 118, 124] As for the spin canting effect, it is important to observe the intensity of the 2^{nd} and 5^{th} peaks in the Mössbauer spectroscopy spectral lines in order to derive the canting angle. [101, 115, 117, 119, 120] It was recently demonstrated in 2011 through Mössbauer spectroscopy that, as the temperature increases, the atomic level spin canting reduces up to a temperature of about 200 K, for γ- Fe_2O_3 nanoparticles of sizes ~ 22 nm. [101] Figure 45 shows Mössbauer spectroscopy spectra of the γ- Fe_2O_3 nanoparticles of sizes ~ 22 nm and ~ 3 nm, measured in 5 Tesla and at various temperatures.

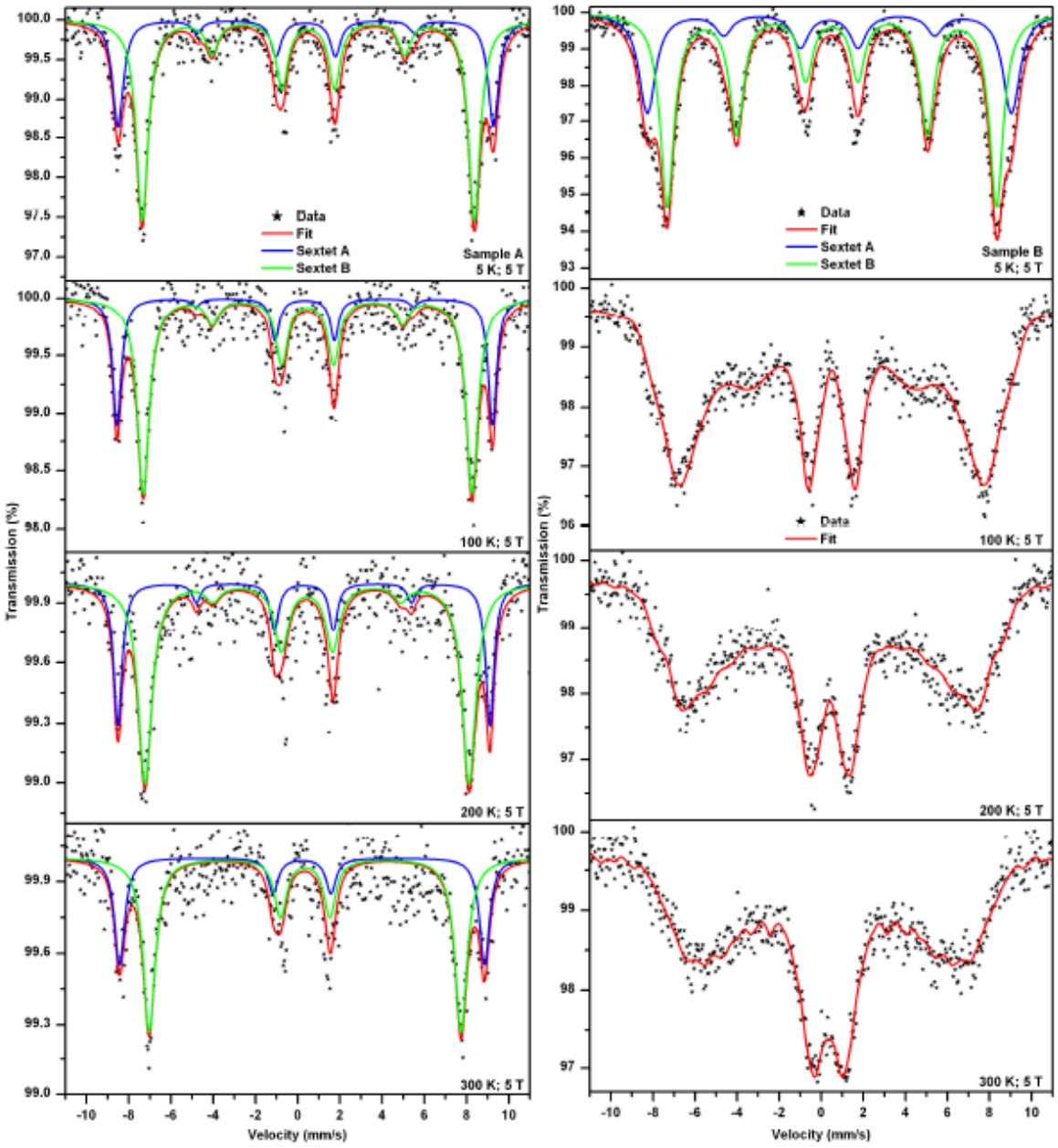
Data
Fit
Sextet A
Sextet B
Sample A
5 K; 5 T
Sample B
5 K; 5 T
100 K; 5 T
200 K; 5 T
300 K; 5 T
Transmission (%)
Velocity (mm/s)

Figure 45. Mössbauer spectra of the γ- Fe_2O_3 nanoparticles of sizes ~ 22 nm (sample A, left 4 graphs) and γ- Fe_2O_3 nanoparticles of sizes ~ 3 nm (sample B, right 4 graphs) at temperatures from 5 K (top) to 300 K (bottom) in a magnetic field of 5 Tesla. [101] Note that the Mössbauer data is taken from Šeděnková et al's work in 2011.

For γ- Fe_2O_3 nanoparticles of sizes ~ 22 nm, the intensity (area) of the 2^{nd} and 5^{th} peak is the highest at the lowest temperature, 5 K, showing a high degree of spin canting. In other words, at very low temperatures, the surface spins are in a disordered state due to large spin canting effect. [101] This reduces the spin-tunneling probability, resulting in an increase in resistance and a decrease in dielectric property. The intensity decreases as we increase the temperature from 5 K to 200 K and the intensity becomes almost negligible at 200 K indicating that spin canting vanishes at around 200 K. [101]

One thing of importance is that spin canting vanishes at around 100 K for γ- Fe_2O_3 nanoparticles of sizes ~ 3 nm, indicating that the spin canting effect significantly depends on particle size as well as the temperature. It should be noted that the size distribution of nanoparticles is another factor which affects the spin canting phenomena since these two groups of nanoparticles, seen in reference [101], have different size distribution data.

When we compare the area of the 2nd and 5th peaks of both particles, the γ- Fe_2O_3 nanoparticles of sizes ~ 3 nm is much larger. This indicates that at low temperature the spin canting is much more prominent for smaller nanoparticles due to the larger surface to volume ratio. As we increase the temperature up to 100 K, the intensity of 2nd and 5th peaks reduced almost to zero, implying that the smaller the magnetic nanoparticles are more susceptible to increases in the temperature. Another point that can be observed in the data for the smaller nanoparticles is that at higher temperatures the magnetic hyperfine splitting collapses to a greater degree. This reflects that the blocking temperature for smaller nanoparticles is much lower than that of the larger nanoparticles. [118] The reason why the magnetic splitting does not disappear completely at temperatures above the blocking temperature, even in the case of extremely small magnetic nanoparticles, is that the measurements are performed in a large magnetic field of 5 Tesla. The observation of the magnetic splitting seen in the Mössbauer spectroscopy results is a well-known characteristic of superparamagnetic nanoparticles. [118] Linderoth et al [118] demonstrated that superparamagnetic Fe-Hg nanoparticles, which did not have any magnetic splitting in their Mössbauer spectra in the case of zero magnetic field, started to show magnetic splitting when a magnetic field is applied.

Considering the data regarding the γ- Fe_2O_3 nanoparticles of sizes ~ 22 nm having negligible spin canting at 200 K, it should be noted that at the atomic level the test conditions favor spin-dependent tunneling which reduces the resistance and increases the dielectric property. Above 200 K, due to thermal agitation, a misalignment in the spins begins to result in a disordered spin state, decreasing the magnetodielectric effect of the system. Therefore hypothetically, a temperature of ~ 200 K for the present system is where the spin-dependent electron tunneling maximizes and the resistance of the sample minimizes leading to a maximum MD %. This explains the maximum of the magnetodielectric coefficient at 200 K. [101]

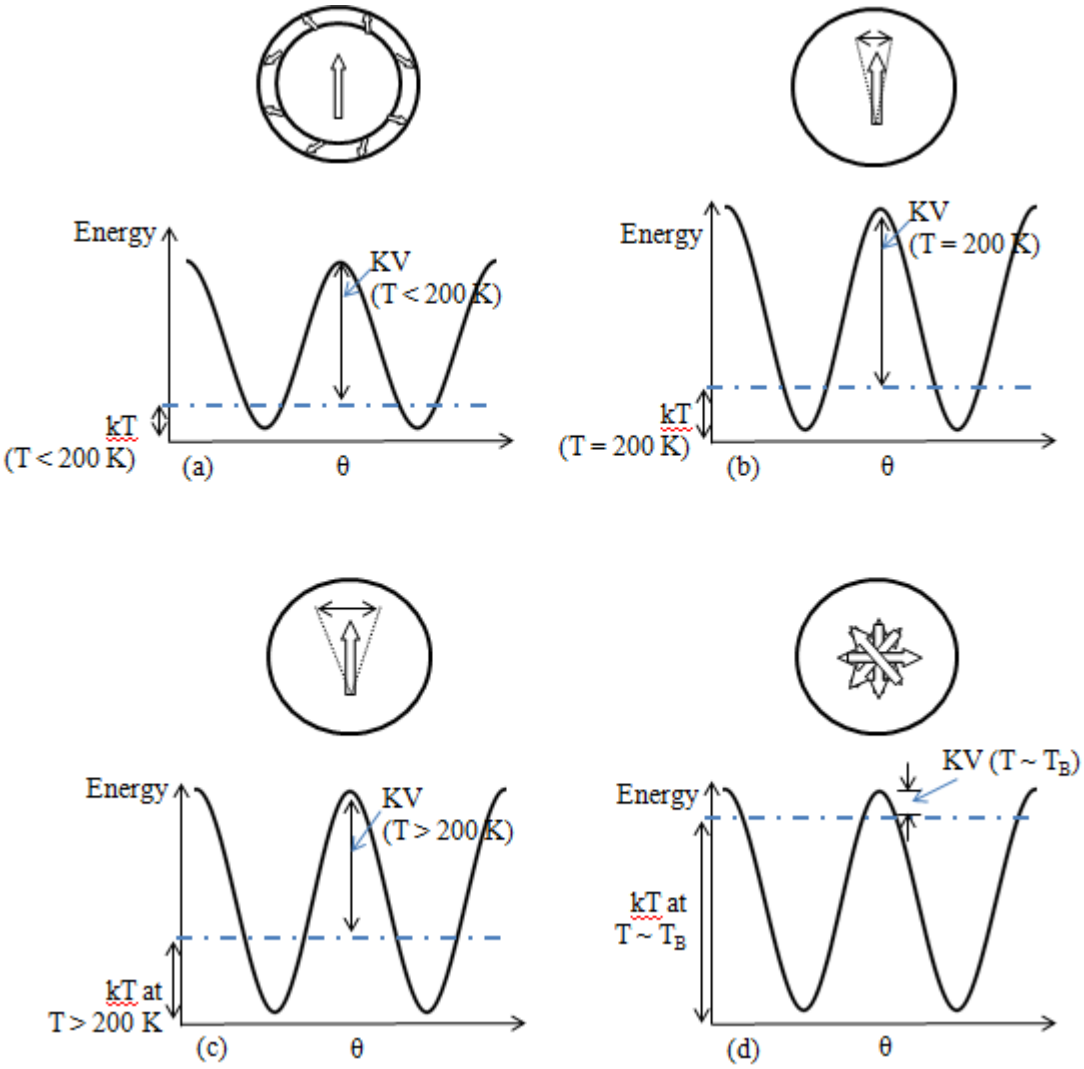

Figure 46. Spin states of nanoparticles and corresponding schematic energy well.

(a) T < 200 K. (b) T = 200 K. (c) T > 200 K. (d) T ~ T_B

Figure 46 shows schematic illustrations of the spin states for the γ- Fe_2O_3 nanoparticles of size ~ 22 nm and their corresponding energy well graphs, in order to explain correlation between spin states and the maximum of magnetic anisotropy using the same philosophy with regard to the temperature effect on spin canting. It is well documented that the effective magnetic anisotropy coefficient is a non linear function of temperature with experimental data recently published for ferrite systems. [114, 125] As can be seen in figure 46 (a), at the low temperatures regime (i.e. T < 200 K) for γ- Fe_2O_3 particles of sizes ~ 22 nm, spin canting exists at the surface of the nanoparticle. Magnetic anisotropy energy, KV is determined by subtracting the thermal energy, kT, from the height of the energy well; K is effective magnetic anisotropy per volume, V is volume of one nanoparticle, k is the Boltzmann constant and T is temperature.

As the temperature was increased up to 200 K, the thickness of the surface containing spin canting gradually decreased and vanished at 200 K as illustrated in the diagram of figure 46 (b). [101] At 200 K, due to the absence of the spin canting, we can think of the spin state of the nanoparticle as a single domain where the magnetization is aligned in the easy axis as it is described in the figure 46 (b). When compared with figure 46 (a), figure 46 (b) shows the thermal agitation of the magnetization, as well as an increased height in the energy well (i.e. as compared to figure 46 (b)), since more spins in

the particles are aligned, increasing KV, which is the energy required to flip the magnetization from one easy axis to another. Therefore, the magnetic anisotropy increased as we approach 200 K. Above 200 K, the change of both spin state and energy well is related to temperature.

Figure 46 (c) shows increased thermal agitation of the magnetization (compared with figure 46 (b)) as well as decreased KV due to the increased kT value while the height of the energy well stays the same. Above 200 K, the magnetic anisotropy decreases with increasing temperature. When the temperature approaches the blocking temperature of the nanoparticle, as shown in figure 46 (d), the nanoparticle becomes superparamagnetic showing randomized flipping of the magnetization. The magnetic anisotropy, KV, accordingly reduces to negligible value since now the thermal energy is comparable to the magnetic anisotropy energy.

4.5 Future work

Since it was previously demonstrated by Bonaedy et al [104] that the dielectric constant of γ- Fe_2O_3 strongly depends on the measuring frequency, more experimentation on varying frequencies would be helpful to strengthen our arguments. Bonaedy et al [104] reported that the ratio of the dielectric constants between frequencies of 10^2 and 10^6 Hz is

approximately 60 at a constant temperature of 293 K. However, they did not address whether the temperature, where the maximum value of the dielectric constant is found, shifts to the higher or lower temperatures depending on the measuring frequencies. If the temperature corresponding to the maximum value of the dielectric constant shifts to different temperatures when measured in different frequencies, we have to address that our argument is only valid under the condition of measuring at our chosen frequency value of 100 kHz.

Furthermore, more experiments varying the size of the nanoparticles would be beneficial in bolstering our report, reflecting on the fact that the temperature in which spin canting vanishes strongly depends on particle size and size distribution. [101] Šeděnková et al's work in 2011 demonstrated that spin canting for γ- Fe_2O_3 particles of sizes ~ 22 nm vanished around 200 K. [101] It should be noted that the size and the size distribution of our γ- Fe_2O_3 nanoparticles varied from those reported in the literature. We purchased the γ- Fe_2O_3 nanoparticles from Alpha Aesar, who claimed that their particles were in the range of 8 to 10 nm. Šeděnková et al used the γ- Fe_2O_3 nanoparticles purchased from Nanophase Technologies Corporation, which showed a wide size distribution from 5 to 80 nm with an average particle diameter of ~ 22 nm. This was determined by a mathematical analysis of TEM images which was in the same range as the values obtained from the XRD pattern

using the Scherrer equation. The size distribution data showed that more than 70 % of the particles used in Šeděnková et al's work are in the range from 10 to 25 nm. [101] The size factor only becomes more convoluted when considering that the agglomeration of the nanoparticles since their magnetic properties might give rise to more size variations with different magnetic behaviors depending on how the fabrication processes are performed. For example, while it is difficult to observe how effective the dispersion processes were, SEM images of the nanoparticles before dispersion processes indicated that the size of the agglomerated nanoparticles could be micron sized. As briefly mentioned above, Šeděnková et al reported that spin canting for γ- Fe_2O_3 nanoparticles of sizes ~ 3 nm vanishes at around 100 K; 100 K lower than that of γ- Fe_2O_3 nanoparticles of sizes ~ 22 nm. [101] Therefore, investigation on the size and size distribution of our nanoparticles are necessary to effectively compare Šeděnková et al's work to our own.

4.6 Summary

Magnetic properties of γ- Fe_2O_3 nanocomposites have been investigated for a wide range of temperatures and applied magnetic fields. Test results show that a maximum in the MD % correlates with a maximum in the effective magnetic anisotropy. While the

correlation was associated with the spin canting effect dominating at temperatures up to 200 K, thermal energy begins to take over above 200 K, which influences MD % as well as K_E. It is speculated that future optimization of magnetic anisotropy may lead to improved MD/ME coupling in single phase magnetoelectric materials.

5. Conclusion

We have studied the magnetoelectric effect and the magnetodielectric effect on magnetic nanoparticles. With respect to the magnetoelectric effect, we discovered that we can turn the observed magnetization on and off (superparamagnetic to single domain state) by applying an electric field induced anisotropic strain to Ni nanoparticles mechanically attached to a piezoelectric substrate. In addition, we observed an increase in the blocking temperature of ~ 40 K which is attributed to the stabilization of the magnetic moments in the nanoparticles. The amount of temperature increase was in a good agreement with the theoretical calculation. We believe that this discovery might lead to a solution to problems associated with magnetic memory. Additionally, the magnetodielectric measurements on γ- Fe_2O_3 revealed that a maximum in the MD % correlates with a maximum in the effective magnetic anisotropy. The results might open up the possibility of designing single phase magnetoelectric materials with a large magnetoelectric coefficient.

References

1. Eerenstein, W., N. Mathur, and J. Scott, *Multiferroic and magnetoelectric materials.* Nature, 2006. **442**(7104): p. 759-765.
2. Röntgen, W.C., *Ueber die durch Bewegung eines im homogenen electrischen Felde befindlichen Dielectricums hervorgerufene electrodynamische Kraft.* Annalen der Physik, 1888. **271**(10): p. 264-270.
3. Debye, P., *Bemerkung zu einigen neuen Versuchen über einen magneto-elektrischen Richteffekt.* Zeitschrift für Physik A Hadrons and Nuclei, 1926. **36**(4): p. 300-301.
4. Astrov, D., *The magnetoelectric effect in antiferromagnetics.* Zh. Eksp. Teor. Fiz, 1960. **38**: p. 984.
5. Folen, V., G. Rado, and E. Stalder, *Anisotropy of the Magnetoelectric Effect in Cr_ {2} O_ {3}.* Physical Review Letters, 1961. **6**(11): p. 607-608.
6. Krichevtsov, B., V. Pavlov, and R. Pisarev, *Giant linear magnetoelectric effect in garnet ferrite films.* JETP Lett, 1989. **49**(8).
7. Wang, K., J.M. Liu, and Z. Ren, *Multiferroicity: the coupling between magnetic and polarization orders.* Advances in Physics, 2009. **58**(4): p. 321-448.
8. Schmid, H., *On a magnetoelectric classification of materials.* Int. J. Magn, 1973. **4**: p. 337-361.
9. Rado, G., J. Ferrari, and W. Maisch, *Magnetoelectric susceptibility and magnetic symmetry of magnetoelectrically annealed TbPO_ {4}.* Physical Review B, 1984. **29**(7): p. 4041.
10. Gehring, G., *On the microscopic theory of the magnetoelectric effect.* Ferroelectrics, 1994. **161**(1): p. 275-285.
11. Fiebig, M., *Revival of the magnetoelectric effect.* Journal of Physics D: Applied Physics, 2005. **38**(8): p. R123.
12. Tellegen, B.D.H., *The gyrator, a new electric network element.* Philips Research Reports, 1948. **3**(2): p. 81-101.
13. Van Den Boomgaard, J., A. Van Run, and J. Van Suchtelen, *Magnetoelectricity in piezoelectric-magnetostrictive composites.* Ferroelectrics, 1976. **10**(1): p. 295-298.
14. Van den Boomgaard, J., A. Van Run, and J. Van Suchtelen, *Piezoelectric-piezomagnetic composites with magnetoelectric effect.* Ferroelectrics, 1976. **14**(1): p. 727-728.
15. Van den Boomgaard, J. and R. Born, *A Sintered Magnetoelectric Composite Material BaTiO3-Ni (Co, Mn) Fe3O4.* J. Mater. Sci, 1978. **13**(5): p. 1538-1548.

16. Van Suchtelen, J., *Product properties: a new application of composite materials.* Philips Res. Rep, 1972. **27**(1): p. 28-37.
17. Nan, C.-W., *Magnetoelectric effect in composites of piezoelectric and piezomagnetic phases.* Physical Review B, 1994. **50**(9): p. 6082-6088.
18. Nan, C., et al., *Multiferroic magnetoelectric composites: Historical perspective, status, and future directions.* Journal of Applied Physics, 2008. **103**: p. 031101.
19. Eerenstein, W., et al., *Giant sharp and persistent converse magnetoelectric effects in multiferroic epitaxial heterostructures.* Nature Materials, 2007. **6**(5): p. 348-351.
20. Ryu, J., et al., *Magnetoelectric properties in piezoelectric and magnetostrictive laminate composites.* Japanese journal of applied physics, 2001. **40**(part 1): p. 4948-4951.
21. Zavaliche, F., et al., *Electric field-induced magnetization switching in epitaxial columnar nanostructures.* Nano letters, 2005. **5**(9): p. 1793-1796.
22. Zavaliche, F., et al., *Electrically assisted magnetic recording in multiferroic nanostructures.* Nano letters, 2007. **7**(6): p. 1586-1590.
23. Chung, T.K., G.P. Carman, and K.P. Mohanchandra, *Reversible magnetic domain-wall motion under an electric field in a magnetoelectric thin film.* Applied Physics Letters, 2008. **92**(11): p. 112509-112509-3.
24. Pyatakov, A., et al., *Electric Field Induced Transformation of Magnetic Domain Structure in Magnetoelectric Iron Garnet Films.* Arxiv preprint arXiv:0806.0811, 2008.
25. Wang, J., et al., *Epitaxial BiFeO3 multiferroic thin film heterostructures.* Science, 2003. **299**(5613): p. 1719-1722.
26. Liu, M., et al., *Strong magnetoelectric coupling in ferrite/ferroelectric multiferroic heterostructures derived by low temperature spin-spray deposition.* Journal of Physics D: Applied Physics, 2009. **42**(4): p. 045007.
27. Liu, M., et al., *Electrical tuning of magnetism in FeO/PZN–PT multiferroic heterostructures derived by reactive magnetron sputtering.* Journal of Applied Physics, 2010. **107**: p. 073916.
28. Li, N., et al., *Electrostatic tuning of ferromagnetic resonance and magnetoelectric interactions in ferrite-piezoelectric heterostructures grown by chemical vapor deposition.* Applied Physics Letters, 2011. **99**(19): p. 192502-192502-3.
29. Zheng, H., et al., *Multiferroic BaTiO3-CoFe2O4 nanostructures.* Science, 2004. **303**(5658): p. 661-663.

30. Wu, T., et al., *Giant electric-field-induced reversible and permanent magnetization reorientation on magnetoelectric Ni/(011)[Pb (MgNb) O]-[PbTiO] heterostructure.* Applied Physics Letters, 2011. **98**: p. 012504.
31. Wu, T., et al., *Electric-poling-induced magnetic anisotropy and electric-field-induced magnetization reorientation in magnetoelectric Ni/(011)[Pb (Mg1/3Nb2/3) O3](1-x)-[PbTiO3] x heterostructure.* Journal of Applied Physics, 2011. **109**: p. 07D732.
32. Wu, T., et al., *Electrical control of reversible and permanent magnetization reorientation for magnetoelectric memory devices*. Vol. 98. 2011: AIP. 262504.
33. Chu, Y.H., et al., *Electric-field control of local ferromagnetism using a magnetoelectric multiferroic.* Nature Materials, 2008. **7**(6): p. 478-482.
34. Chung, T.-K., S. Keller, and G.P. Carman, *Electric-field-induced reversible magnetic single-domain evolution in a magnetoelectric thin film.* Applied Physics Letters, 2009. **94**(13): p. 132501.
35. Bur, A., et al., *Strain-induced magnetization change in patterned ferromagnetic nickel nanostructures.* Journal of Applied Physics, 2011. **109**(12): p. 123903.
36. Kittel, C., *Physical theory of ferromagnetic domains.* Reviews of Modern Physics, 1949. **21**(4): p. 541.
37. Frenkel, J. and J. Doefman, *Spontaneous and induced magnetisation in ferromagnetic bodies.* Nature, 1930. **126**(3173): p. 274-275.
38. Kittel, C., *Theory of the structure of ferromagnetic domains in films and small particles.* Physical Review, 1946. **70**(11-12): p. 965.
39. Bedanta, S. and W. Kleemann, *Supermagnetism.* Journal of Physics D: Applied Physics, 2009. **42**: p. 013001.
40. Leslie-Pelecky, D.L. and R.D. Rieke, *Magnetic properties of nanostructured materials.* Chem. Mater, 1996. **8**(8): p. 1770-1783.
41. Jun, Y., J. Seo, and J. Cheon, *Nanoscaling laws of magnetic nanoparticles and their applicabilities in biomedical sciences.* Accounts of chemical research, 2008. **41**(2): p. 179-189.
42. Cowburn, R., *Superparamagnetism and the future of magnetic random access memory.* Journal of Applied Physics, 2003. **93**: p. 9310.
43. Bean, C. and J. Livingston, *Superparamagnetism.* Journal of Applied Physics, 1959. **30**(4): p. S120-S129.
44. Knobel, M., et al., *Superparamagnetism and other magnetic features in granular materials: A review on ideal and real systems.* Journal of Nanoscience and Nanotechnology, 2008. **8**(6): p. 2836-2857.

45. Néel, L., *Influence des fluctuations thermiques sur l'aimantation de grains ferromagnétiques très fins.* CR Acad. Sci, 1949. **228**: p. 664-668.
46. Bean, C., *Hysteresis loops of mixtures of ferromagnetic micropowders.* Journal of Applied Physics, 1955. **26**(11): p. 1381-1383.
47. Gunn, J.W., *The preparation and characterization of superparamagnetic nanoparticles for biomedical imaging and therapeutic application*. 2008: ProQuest.
48. Chen, Q. and Z.J. Zhang, *Size-dependent superparamagnetic properties of MgFeO spinel ferrite nanocrystallites.* Applied Physics Letters, 1998. **73**: p. 3156.
49. Neuberger, T., et al., *Superparamagnetic nanoparticles for biomedical applications: Possibilities and limitations of a new drug delivery system.* Journal of Magnetism and Magnetic Materials, 2005. **293**(1): p. 483-496.
50. Berry, C.C., *Possible exploitation of magnetic nanoparticle–cell interaction for biomedical applications.* J. Mater. Chem., 2004. **15**(5): p. 543-547.
51. Yang, J.K.W., et al., *Fabrication and characterization of bit-patterned media beyond 1.5 Tbit/in2.* Nanotechnology, 2011. **22**(38): p. 385301.
52. White, R.L., *The physical boundaries to high-density magnetic recording.* Journal of Magnetism and Magnetic Materials, 2000. **209**(1): p. 1-5.
53. Hellwig, O., et al., *Bit patterned media based on block copolymer directed assembly with narrow magnetic switching field distribution.* Applied Physics Letters, 2010. **96**(5): p. 052511-052511-3.
54. Hong, A.J., et al., *Metal nanodot memory by self-assembled block copolymer lift-off.* Nano letters, 2009. **10**(1): p. 224-229.
55. Xiao, S., et al., *Aligned nanowires and nanodots by directed block copolymer assembly.* Nanotechnology, 2011. **22**: p. 305302.
56. Skumryev, V., et al., *Beating the superparamagnetic limit with exchange bias.* Nature, 2003. **423**(6942): p. 850-853.
57. Tamion, A., et al., *Magnetic anisotropy of embedded Co nanoparticles: Influence of the surrounding matrix.* Physical Review B, 2010. **81**(14): p. 144403.
58. Nogues, J. and I.K. Schuller, *Exchange bias.* Journal of Magnetism and Magnetic Materials, 1999. **192**(2): p. 203-232.
59. Eisenmenger, J. and I.K. Schuller, *Overcoming thermal fluctuations.* Nat Mater, 2003. **2**: p. 437-438.
60. Singh, M.P., et al., *Magnetocapacitance effect in perovskite-superlattice based multiferroics.* Applied Physics Letters, 2005. **87**(2): p. 022505-3.
61. Catalan, G., *Magnetocapacitance without magnetoelectric coupling.* Applied Physics Letters, 2006. **88**: p. 102902.

62. Kimura, T., et al., *Magnetocapacitance effect in multiferroic BiMnO_{3}.* Physical Review B, 2003. **67**(18): p. 180401.
63. Hur, N., et al., *Colossal Magnetodielectric Effects in DyMn_ {2} O_ {5}.* Physical Review Letters, 2004. **93**(10): p. 107207.
64. Lawes, G., et al., *Positive and negative magnetocapacitance in magnetic nanoparticle systems.* Applied Physics Letters, 2006. **88**(24): p. 242903-3.
65. Grigorescu, A. and C. Hagen, *Resists for sub-20-nm electron beam lithography with a focus on HSQ: state of the art.* Nanotechnology, 2009. **20**(29): p. 292001.
66. Hyeon, T., *Chemical synthesis of magnetic nanoparticles.* Chem. Comm., 2003: p. 927-934.
67. Park, J., et al., *Ultra-large-scale syntheses of monodisperse nanocrystals.* Nat Mater, 2004. **3**(12): p. 891-895.
68. Evans, P., et al., *Growth and properties of gold and nickel nanorods in thin film alumina.* Nanotechnology, 2006. **17**: p. 5746.
69. Masuda, H. and M. Satoh, *Fabrication of gold nanodot array using anodic porous alumina as an evaporation mask.* Japanese journal of applied physics, 1996. **35**(1B): p. L126-L129.
70. Lei, Y. and W.K. Chim, *Shape and size control of regularly arrayed nanodots fabricated using ultrathin alumina masks.* Chem. Mater, 2005. **17**(3): p. 580-585.
71. Jung, J.S., et al., *Electrodeposited Nickel Nanodots Array on the Silicon Wafer.* Bull. Korean Chem. Soc, 2008. **29**(11): p. 2169.
72. Wang, Y., et al., *High-density arrays of InGaN nanorings, nanodots, and nanoarrows fabricated by a template-assisted approach.* The Journal of Physical Chemistry B, 2006. **110**(23): p. 11081-11087.
73. Pan, C. and J. Zhu, *The syntheses, properties and applications of Si, ZnO, metal, and heterojunction nanowires.* J. Mater. Chem., 2009. **19**(7): p. 869-884.
74. Lee, W., et al., *Fast fabrication of long-range ordered porous alumina membranes by hard anodization.* Nat Mater, 2006. **5**(9): p. 741-747.
75. Huang, C.-H., et al., *Optical characteristics of pore size on porous anodic aluminium oxide films with embedded silver nanoparticles.* Sensors and Actuators A: Physical, 2012. **180**(0): p. 49-54.
76. Hu, G., et al., *Study on Wet Etching of AAO Template.* Applied Physics Research, 2009. **1**(2): p. P78.
77. Taşaltın, N., et al., *Simple fabrication of hexagonally well-ordered AAO template on silicon substrate in two dimensions.* Applied Physics A: Materials Science & Processing, 2009. **95**(3): p. 781-787.

78. Liang, J., H. Chik, and J. Xu, *Nonlithographic fabrication of lateral superlattices for nanometric electromagnetic-optic applications.* Selected Topics in Quantum Electronics, IEEE Journal of, 2002. **8**(5): p. 998-1008.
79. Tang, C., et al., *Evolution of block copolymer lithography to highly ordered square arrays.* Science, 2008. **322**(5900): p. 429-432.
80. Xia, G., S. Wang, and S.J. Jeong, *A universal approach for template-directed assembly of ultrahigh density magnetic nanodot arrays.* Nanotechnology, 2010. **21**: p. 485302.
81. Hamley, I., *Nanostructure fabrication using block copolymers.* Nanotechnology, 2003. **14**: p. R39.
82. Guarini, K., et al., *Nanoscale patterning using self-assembled polymers for semiconductor applications.* Journal of Vacuum Science & Technology B: Microelectronics and Nanometer Structures, 2001. **19**: p. 2784.
83. Kang, G.B., et al., *Silicon nanodot arrays patterned using diblock copolymer templates.* Journal of electroceramics, 2009. **23**(2): p. 524-529.
84. Jeong, U., et al., *Volume contractions induced by crosslinking: A novel route to nanoporous polymer films.* Advanced Materials, 2003. **15**(15): p. 1247-1250.
85. Kang, G., et al., *Fabrication of silicon nanodots on insulator using block copolymer thin film.* Current Applied Physics, 2009. **9**(2): p. e197-e200.
86. Chen, Y., et al., *Preparation and magnetic properties of nickel nanoparticles via the thermal decomposition of nickel organometallic precursor in alkylamines.* Nanotechnology, 2007. **18**: p. 505703.
87. Lee, K. and S.H. Kang, *Development of embedded STT-MRAM for mobile system-on-chips.* Magnetics, IEEE Transactions on, 2011. **47**(1): p. 131-136.
88. Ramesh, R. and N.A. Spaldin, *Multiferroics: progress and prospects in thin films.* Nat Mater, 2007. **6**(1): p. 21-29.
89. Hu, J.M., et al., *Electric-field control of strain-mediated magnetoelectric random access memory.* Journal of Applied Physics, 2010. **107**(9): p. 093912-093912-10.
90. Lee, K. and S.H. Kang, *Design consideration of magnetic tunnel junctions for reliable high-temperature operation of STT-MRAM.* Magnetics, IEEE Transactions on, 2010. **46**(6): p. 1537-1540.
91. Rottmayer, R.E., et al., *Heat-assisted magnetic recording.* Magnetics, IEEE Transactions on, 2006. **42**(10): p. 2417-2421.
92. McDaniel, T.W., *Ultimate limits to thermally assisted magnetic recording.* Journal of Physics: Condensed Matter, 2005. **17**: p. R315.

93. Hu, J.M., et al., *High-density magnetoresistive random access memory operating at ultralow voltage at room temperature.* Nature Communications, 2011. **2**: p. 553.
94. Pertsev, N. and H. Kohlstedt, *Magnetic tunnel junction on a ferroelectric substrate.* Applied Physics Letters, 2009. **95**: p. 163503.
95. Hu, J.-M. and C.W. Nan, *Electric-field-induced magnetic easy-axis reorientation in ferromagnetic/ferroelectric layered heterostructures.* Physical Review B, 2009. **80**(22): p. 224416.
96. Shevchenko, E.V., et al., *Structural characterization of self-assembled multifunctional binary nanoparticle superlattices.* Journal of the American Chemical Society, 2006. **128**(11): p. 3620-3637.
97. Weiler, M., et al., *Voltage controlled inversion of magnetic anisotropy in a ferromagnetic thin film at room temperature.* New Journal of Physics, 2009. **11**: p. 013021.
98. Hansen, M.F. and S. Mørup, *Estimation of blocking temperatures from ZFC/FC curves.* Journal of Magnetism and Magnetic Materials, 1999. **203**(1-3): p. 214-216.
99. Yoon, M., et al., *Superparamagnetic properties of nickel nanoparticles in an ion-exchange polymer film.* Materials chemistry and physics, 2005. **91**(1): p. 104-107.
100. Guimarães, A.P., *Magnetic Recording.* Principles of Nanomagnetism, 2009: p. 173-184.
101. ŠEDĚNKOVÁ, V., et al., *SPIN CANTING OF γ-Fe2O3 NANOPARTICLES AND ITS EVALUATION EMPLOYING A STATISTICAL APPROACH.*
102. Bonaedy, T., et al., *Resistive magnetodielectric property of polycrystalline gamma-Fe[sub 2]O[sub 3].* Applied Physics Letters, 2007. **91**(13): p. 132901.
103. Koo, Y., et al., *Magnetodielectric coupling in core/shell BaTiO 3/γ-Fe 2 O 3 nanoparticles.* Applied Physics Letters, 2007. **91**(21): p. 212903-212903-3.
104. Bonaedy, T., et al., *Effect of grain boundary on resistive magnetodielectric property of polycrystalline γ-Fe 2 O 3.* Applied Physics A: Materials Science & Processing, 2008. **93**(2): p. 517-520.
105. Mostovoy, M., et al., *Temperature-Dependent Magnetoelectric Effect from First Principles.* Physical Review Letters, 2010. **105**(8): p. 87202.
106. Banerjee, I., et al., *Preparation of γ-Fe< sub> 2</sub> O< sub> 3</sub> nanoparticles using DC thermal arc-plasma route, their characterization and magnetic properties.* Scripta materialia, 2006. **54**(7): p. 1235-1240.
107. Wang, Q., et al., *One-step synthesis of the nanometer particles of γ-Fe2O3 by wire electrical explosion method.* Materials Research Bulletin, 2001. **36**(3–4): p. 503-509.

108. Coey, J. and D. Khalafalla, *Superparamagnetic gamma-Fe2O3.* Physica Status Solidi Applied Research, 1972. **11**: p. 229-241.
109. Leite, E., et al. *Spin-glass-like characteristics of extremely small γ-Fe2O3 nanoparticles*. in *Journal of Physics: Conference Series*. 2010: IOP Publishing.
110. Gangopadhyay, S., et al., *Effect of oxide layer on the hysteresis behavior of fine Fe particles.* Journal of Applied Physics, 1991. **70**(10): p. 5888-5890.
111. Gangopadhyay, S., et al., *Magnetic properties of ultrafine iron particles.* Physical Review B, 1992. **45**(17): p. 9778.
112. Hou, D., X. Nie, and H. Luo, *Studies on the magnetic viscosity and the magnetic anisotropy of γ-Fe2O3 powders.* Applied Physics A: Materials Science & Processing, 1998. **66**(1): p. 109-114.
113. Hou, D.L., X.F. Nie, and H.L. Luo, *Magnetic anisotropy and coercivity of ultrafine iron particles.* Journal of Magnetism and Magnetic Materials, 1998. **188**(1): p. 169-172.
114. Ranvah, N., et al., *Temperature dependence of magnetic anisotropy of Ga-substituted cobalt ferrite.* Journal of Applied Physics, 2008. **103**(7): p. 07E506-07E506-3.
115. Serna, C., et al., *Spin frustration in maghemite nanoparticles.* Solid state communications, 2001. **118**(9): p. 437-440.
116. Papaefthymiou, G.C., *Nanoparticle magnetism.* Nano Today, 2009. **4**(5): p. 438-447.
117. Darbandi, M., et al., *Nanoscale size effect on surface spin canting in iron oxide nanoparticles synthesized by the microemulsion method.* Journal of Physics D: Applied Physics, 2012. **45**(19): p. 195001.
118. Linderoth, S., et al., *A Mössbauer spectroscopy study of superparamagnetism in the iron-mercury system.* Le Journal de Physique Colloques, 1988. **49**(C8): p. 8-8.
119. Morales, M.P., et al., *Surface and Internal Spin Canting in γ-Fe2O3 Nanoparticles.* Chemistry of Materials, 1999. **11**(11): p. 3058-3064.
120. Roca, A., et al., *Magnetite nanoparticles with no surface spin canting.* Journal of Applied Physics, 2009. **105**(11): p. 114309-114309-7.
121. Pankhurst, Q. and R. Pollard, *Origin of the spin-canting anomaly in small ferrimagnetic particles.* Physical Review Letters, 1991. **67**(2): p. 248-250.
122. Boyer, C., et al., *The design and utility of polymer-stabilized iron-oxide nanoparticles for nanomedicine applications.* NPG Asia Materials, 2010. **2**(1): p. 23-30.
123. Pollard, R., *The spin-canting anomaly in ferrimagnetic particles.* Journal of Physics: Condensed Matter, 1999. **2**(4): p. 983.

124. Amulyavichus, A. and I. Suzdalev, *Investigation of the superparamagnetic properties of ultrafine iron particles by Mössbauer spectroscopy.* Soviet Journal of Experimental and Theoretical Physics, 1973. **37**: p. 859.
125. Ranvah, N., et al., *Temperature dependence of magnetic anisotropy of germanium/cobalt cosubstituted cobalt ferrite.* Journal of Applied Physics, 2009. **105**(7): p. 07A518-07A518-3.